Supporting Information

Surface-Confined Macrocyclization via Dynamic Covalent Chemistry

Chaoying Fu,[1,2,7] Jiří Mikšátko,[3] Lea Assies,[3] Vladimír Vrkoslav,[4] Silvia Orlandi,[5] Martin Kalbáč,[3] Petr Kovaříček,[3] Xiaobin Zeng,[1] Boping Zhou,[1] Luca Muccioli,[5,6] Dmitrii F. Perepichka,[7] Emanuele Orgiu[2]

[1] *Center Lab of Longhua Branch and Department of Infectious disease, Shenzhen People's Hospital, 2nd Clinical Medical College of Jinan University, Shenzhen 518120, Guangdong Province, China.*

[2] *INRS, Énergie Matériaux Télécommunications Centre, 1650 boulevard Lionel-Boulet, Varennes (Québec) J3X 1S2, Canada*

[3] *J. Heyrovsky Institute of Physical Chemistry of the Czech Academy of Sciences, Dolejškova 2155/3, 182 23 Praha, Czech Republic*

[4] *Institute of Organic Chemistry and Biochemistry of the Czech Academy of Sciences, Flemingovo náměstí 542/2, 166 10 Praha, Czech Republic*

[5] *Dipartimento di Chimica Industriale "Toso Montanari", Università di Bologna, 40136, Bologna, Italy*
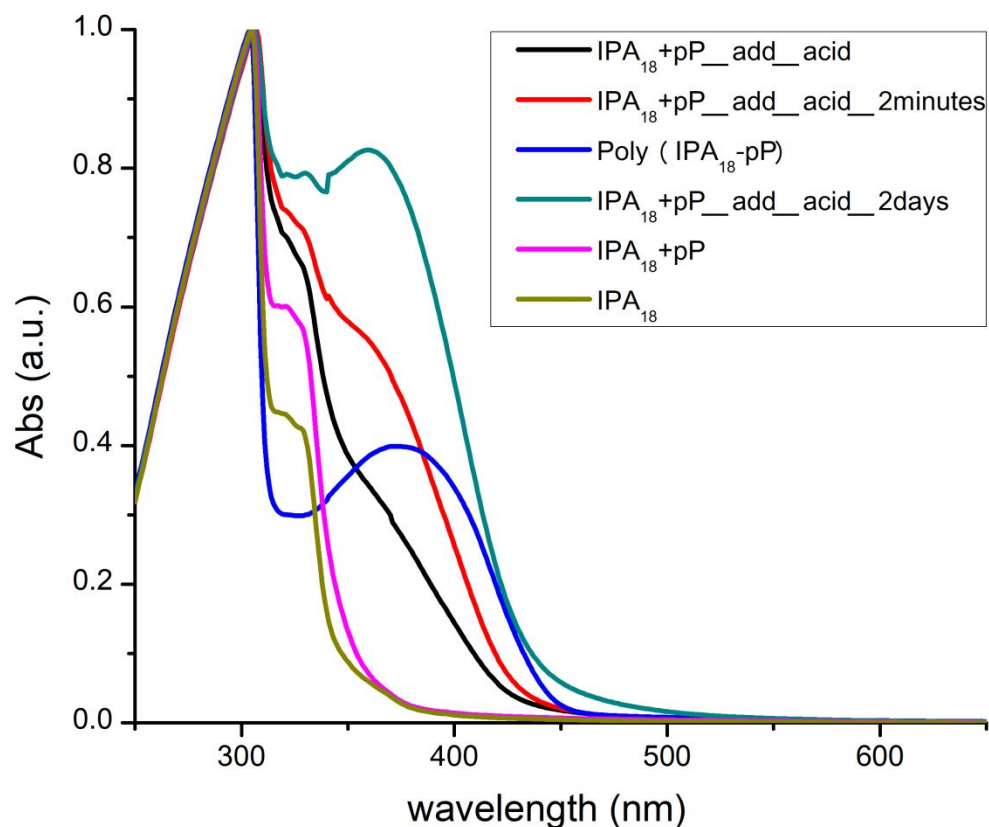
[6] *Institut des Sciences Moléculaires, UMR 5255, University of Bordeaux, 33405 Talence, France*

[7] *Department of Chemistry, McGill University, 801 Sherbrooke Street W., Montreal, QC, Canada H3A 0B8*

# Contents

1. UV-Vis absorption measurements

Fig. S1.1 UV-vis absorption spectra of the *in-situ* reaction of IPA$_{18}$ and pP (0.1 mM each) in TCB measured immediately (**black**), 2 minutes later (**red**) and two days later (**cyan**), as compared to the spectra of the *ex-situ* synthesized (IPA$_{18}$-pP)$_n$ polymers in TCB (**blue**), *in-situ* reaction mixture without adding octanoic acid (**pink**) and IPA$_{18}$ (0.1mM) solution in TCB (**olive green**). The *in-situ* reaction mixture of IPA$_{18}$ and pP was prepared as a premix of IPA$_{18}$ and pP solution (0.2mL each, and 1mM each in TCB; 0.1% v/v DMF in pP solution to ensure its solubilisation in TCB), followed by dilution up to 2mL total volume in TCB and then addition of 50µL octanoic acid.
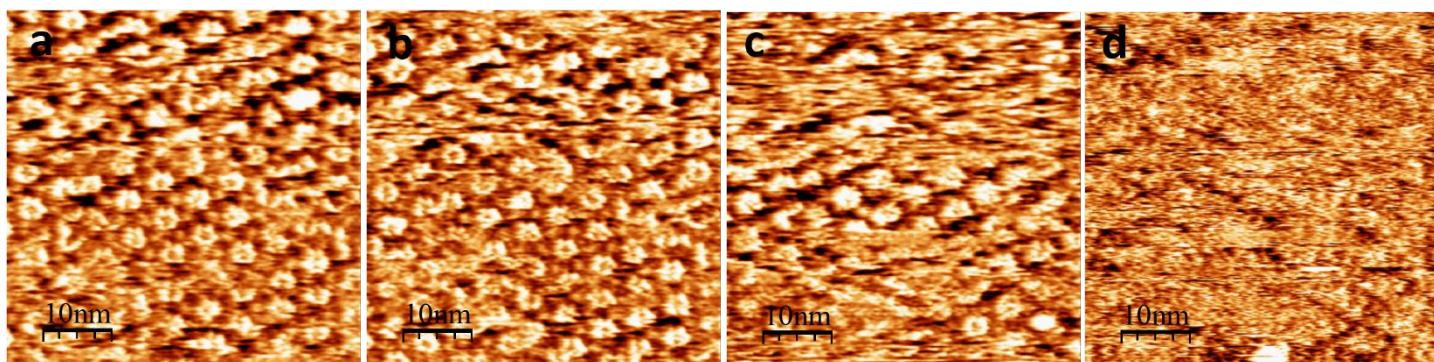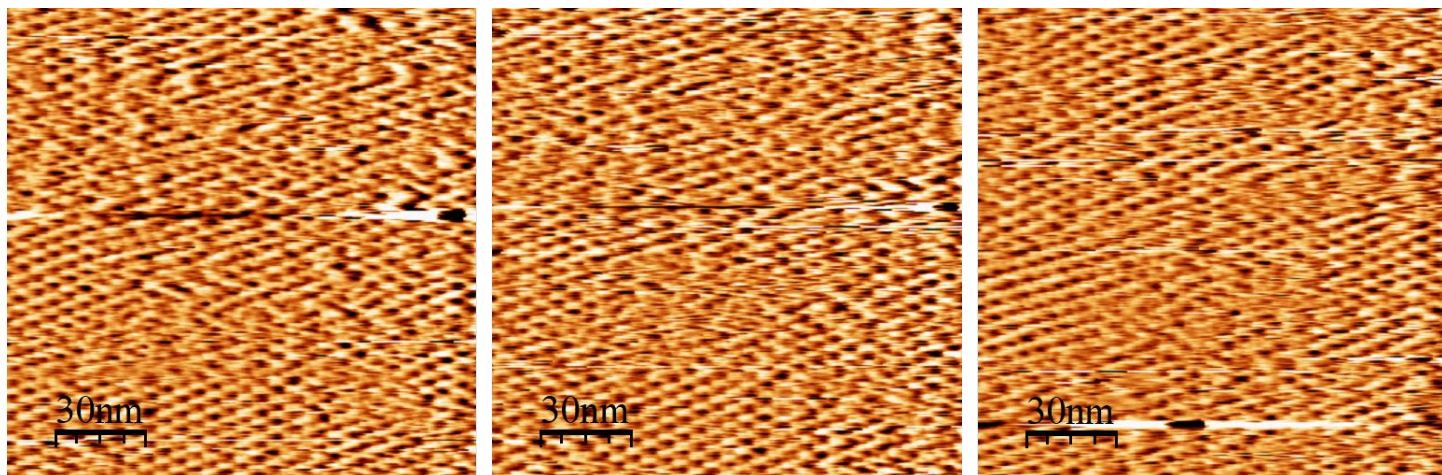
2. Additional STM images

2.1   In-situ polymerization of IPA$_{18}$ and pP
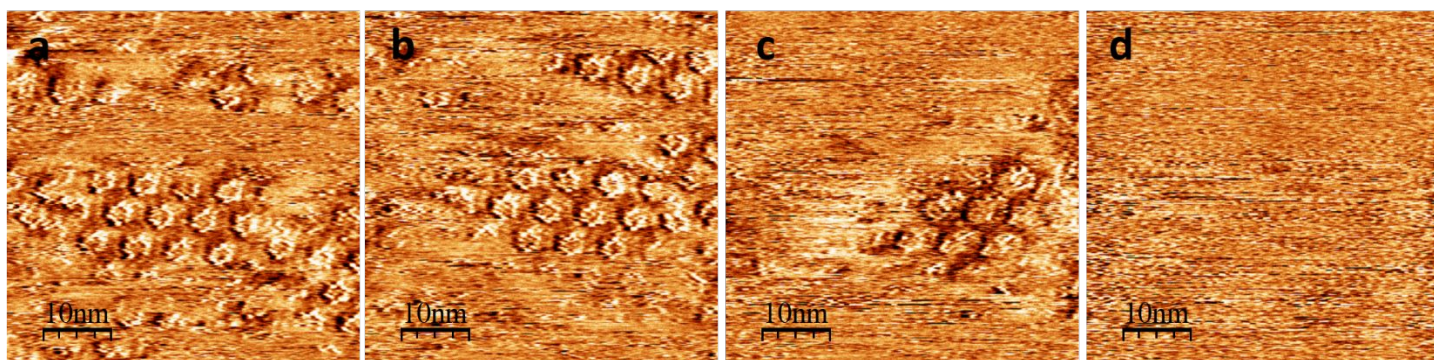
Fig. S2.1-1 (a)-(d) Four consecutive STM images recorded in 120s show in-situ generated macrocycles from IPA$_{18}$ and pP condensation at the TCB/HOPG interface. The formed monolayer was disrupted at high scanning current (160 pA).

Fig. S2.1-2 (a)-(d) Four consecutive STM images recorded in 120s show in-situ generated macrocycles from IPA$_{18}$ and pP condensation at the TCB/HOPG interface. The formed monolayer was disrupted at moderate scanning current (50 pA).

Fig. S2.2 (a)-(c) Three consecutive STM images recorded in 120s show in-situ generated macrocycles from IPA$_{18}$ and pP condensation at the TCB/HOPG interface. The formed macrocycle array was stable at low scanning current (5pA).
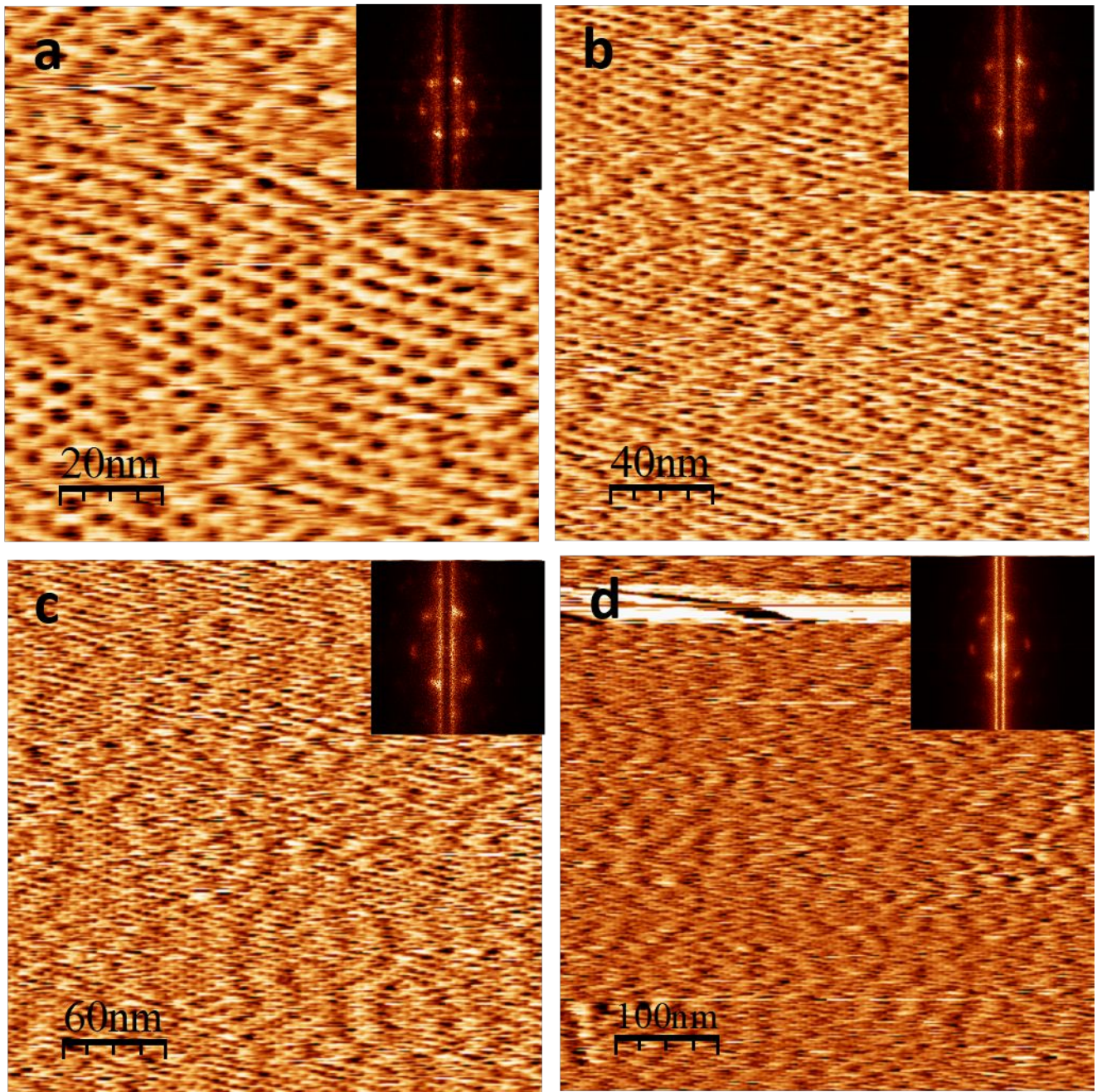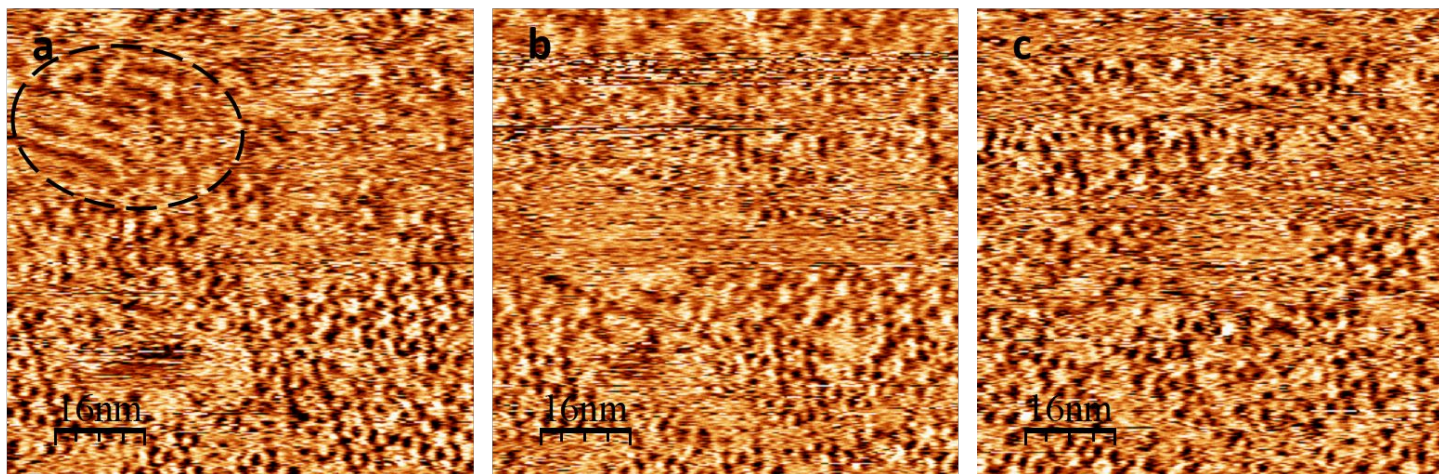
Fig. S2.3 (a)-(d) STM image of large single domain from 100×100 nm^2, 200×200 nm^2 , 300×300 nm^2 to 500×500 nm^2 size with 2D-FFT onset showing a single domain orientation.

Fig. S2.4 Three consecutive STM images of in-situ reaction of IPA$_{18}$ with pP at the TCB/HOPG interface. (a) Co-existence of zigzag linear polymers and macrocyclic products. (b)-(c) Linear polymers disappeared, leaving macrocycles as the main product at the surface.
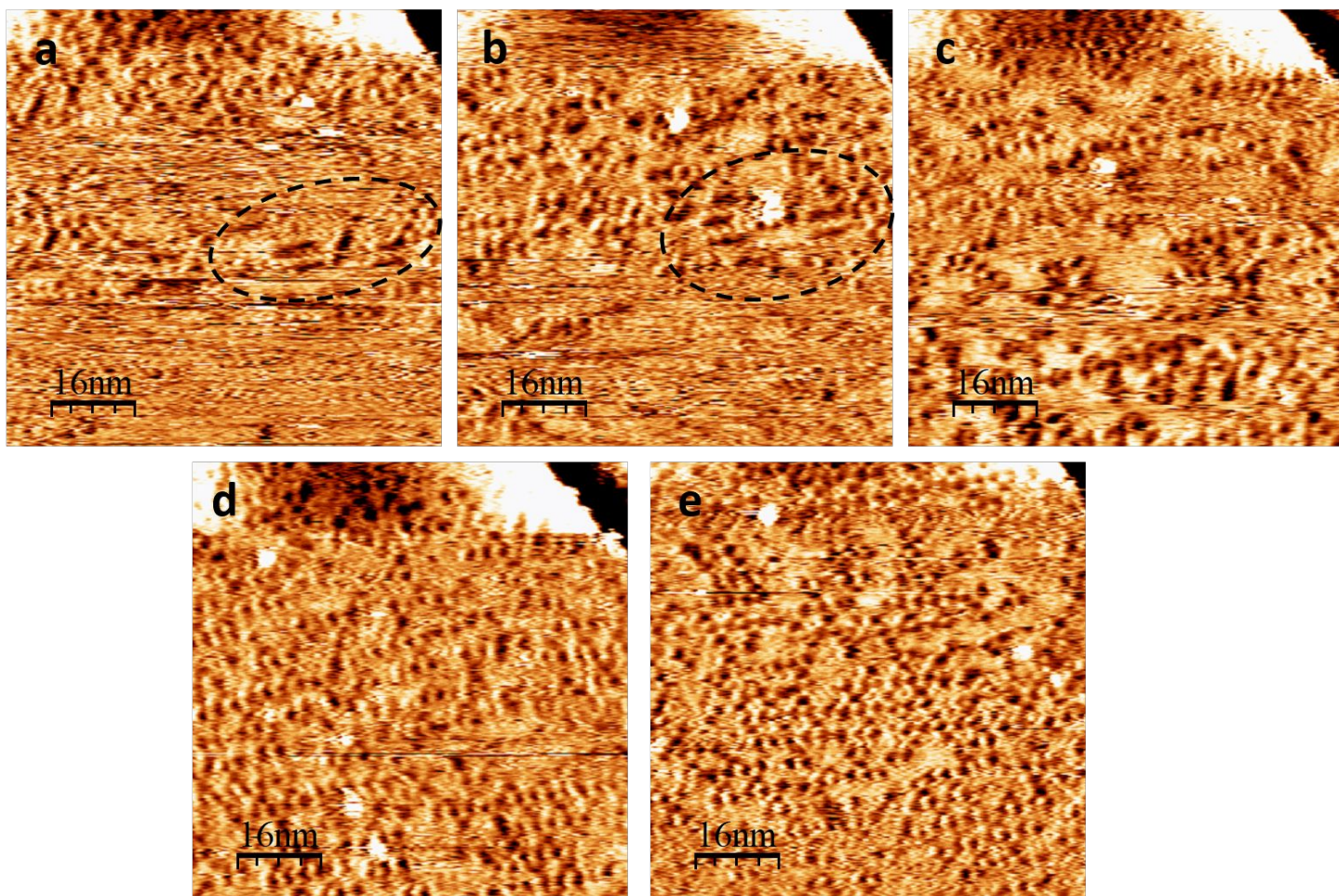
Fig. S2.5 Five consecutive STM images of in-situ reaction of IPA$_{18}$ with pP at the TCB/HOPG. (a)-(b) Co-existence of zigzag linear polymers and macrocyclic products. (c)-(e) Linear polymers disappeared, leaving macrocycles as the main product at the surface.

2.2 Concentration and time dependant in-situ polymerization of IPA_n and pP

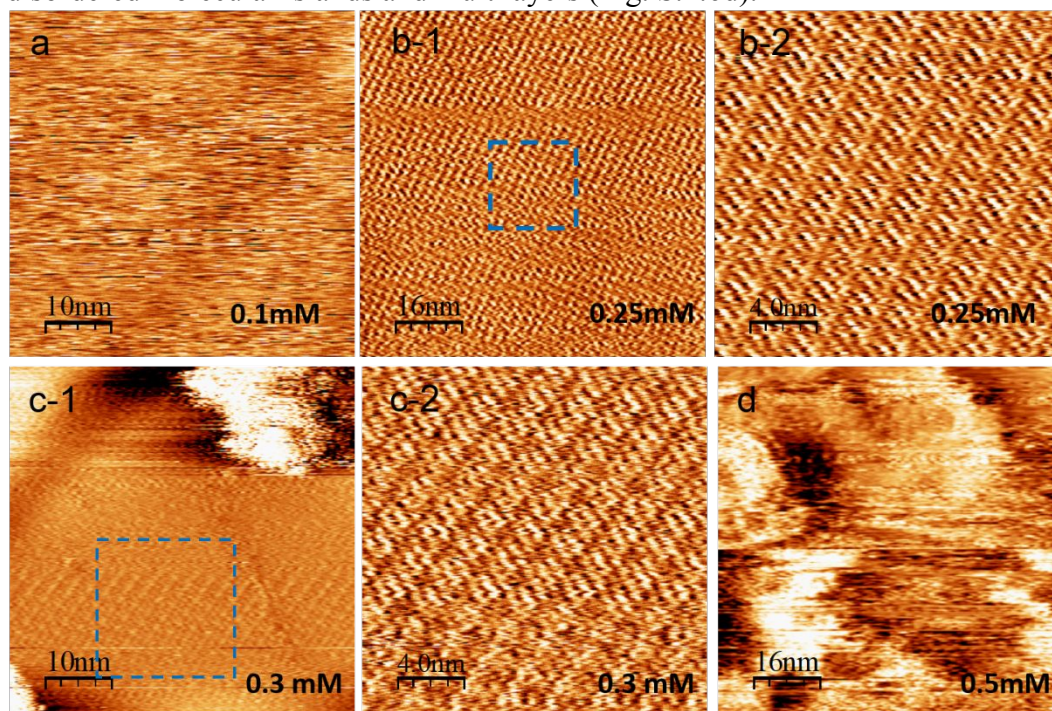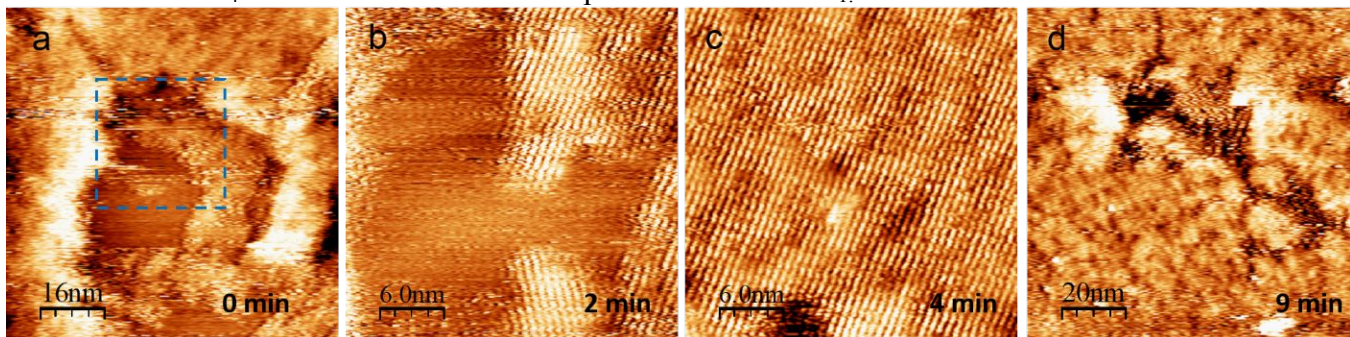**On-surface reaction of IPA_1 + pP :** When drop-casting reaction mixture of 0.25 mM onto HOPG, the close-packed lamellae emerged on the surface and extended over hundred nanometer size (Fig. S.2.6b-1). Increasing the concentration to 0.3 mM led to co-existence of disordered molecular islands and close-packed lamellae on the surface (Fig. S2.6c-1). Further increasing the concentration up to 0.5mM resulted an exclusive formation of disordered molecular islands and multilayers (Fig. S.2.6d).

Fig. S2.6 STM images of the on-surface products of IPA_1 and pP reaction mixture at 0.1 mM (a), 0.25 mM (b-1, b-2), 0.3 mM (c-1, c-2) and 0.5 mM (d). The blue squares in (b-1) and (c-1) refer to the zoomed areas presented in (b-2) and (c-2).

On-surface reaction of IPA_4 + pP : When drop-casting reaction mixture of 0.21 mM onto HOPG, both disordered molecular islands and close-packed lamellae co-existed on the surface (Fig. S2.7a). Tracking on the area partially covered with close-packed lamellae, the lamellae quickly fully covered the surface in a few minutes (Fig. S2.7c). Furthermore, within 9 min, more oligomers were formed and aggregated on the surface, forming disordered islands all over the surface (Fig. S2.7d). Thus it can be learnt that the close-packed lamella network formed from IPA_4 is much less stable as compared to that of IPA_1.

Fig. S2.7 STM images of the on-surface products of IPA_4 and pP reaction mixture at 0 min (a), 2 min (b), 4 min (c) and 9 mM (d). The blue squared area in (a) was tracked and zoomed in (b).
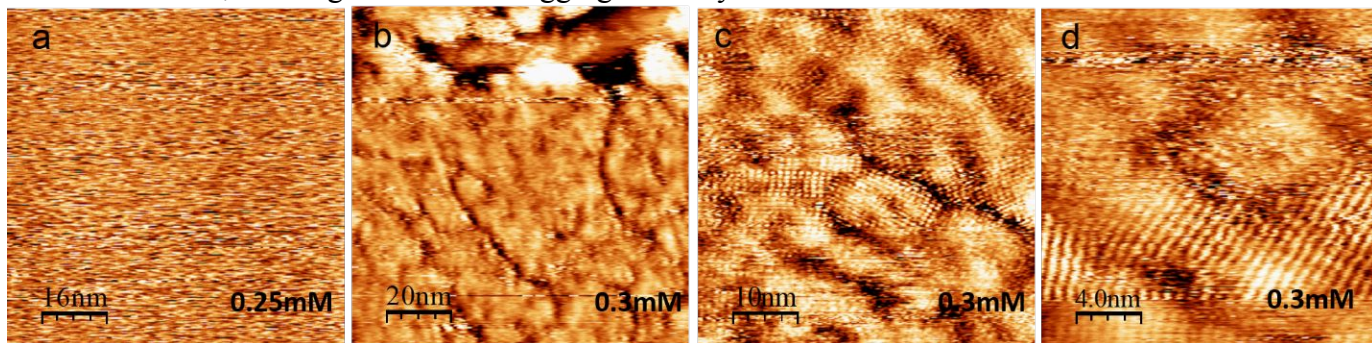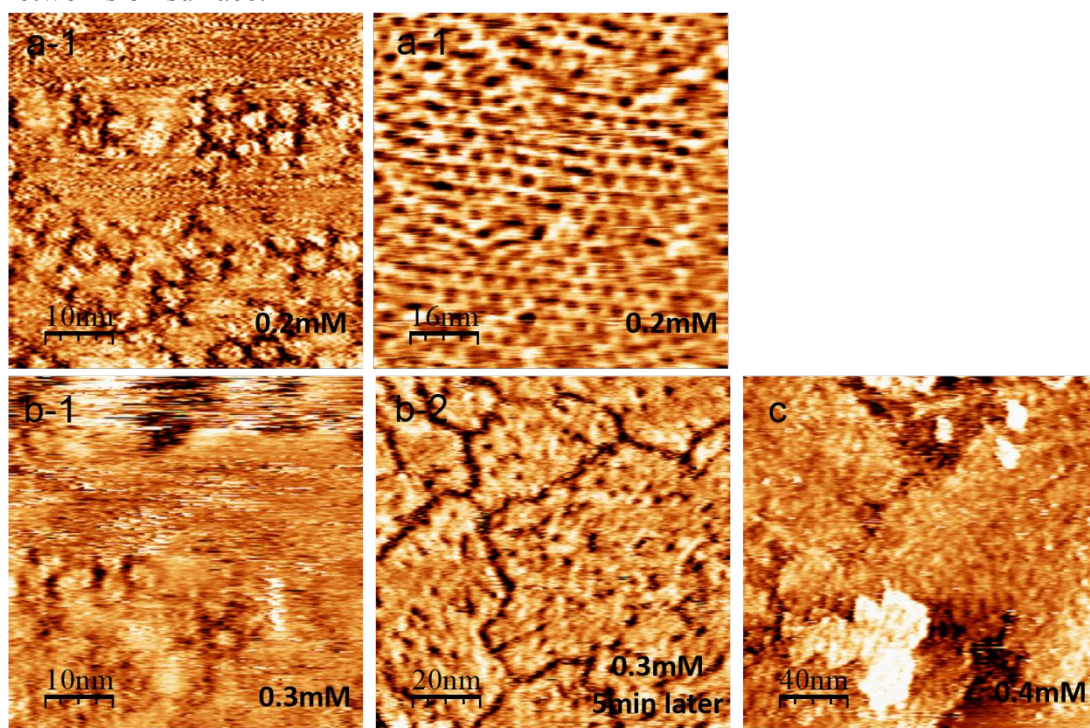
On-surface reaction of IPA$_8$ + pP : When drop-casting reaction mixture of 0.3mM onto HOPG, disordered molecular islands immediately appeared on the surface (Fig. S2.8b). Continuous STM scanning helped to remove some disordered products and the close-packed lamellae were observed (Fig. S2.8c, d), but the stable imaging condition was difficult to obtain. It can be learnt that the lamellae formed by IPA$_8$ is much less stable than those of IPA$_1$ and IPA$_4$. The oligomers tend to aggregate easily on surface.

Fig. S2.8 STM images of the on-surface products of IPA$_8$ and pP reaction mixture at 0.25 mM (a), 0.3 mM (b-d).

On-surface reaction of IPA$_{12}$ + pP : When drop-casting reaction mixture of 0.2 mM onto HOPG, macrocycle network emerged on the surface that was captured at both high and low scanning current (Fig. S2.9a). Increasing the concentration up to 0.3mM, features similar to macrocycles first appeared on the surface (Fig. S2.9b-1), and then the surface was quickly covered with disordered molecular aggregates within 5 min (Fig. S2.9b-2). Further increasing the concentration up to 0.4mM resulted an exclusive formation of disordered molecular islands and multilayers (Fig. S2.9c). Thus it can be learnt that the applied concentration is crucial to achieve macrocycle networks on surface.

Fig. S2.9 STM images of the on-surface products of IPA$_{12}$ and pP reaction mixture at 0.2mM at high (a-1) and low current (a-2), at 0.3mM (b-1) and scanned 5 min later (b-2), and at 0.4mM (c).

On-surface reaction of IPA$_{18}$ + pP : When drop-casting reaction mixture of 0.1 mM onto HOPG, macrocycle network emerged on the surface that was stably captured at low scanning current (Fig. S2.10a-c). The images were recorded continuously in 3 hours, indicating the macrocycle network could remain at the HOPG/TCB interface for a long time.
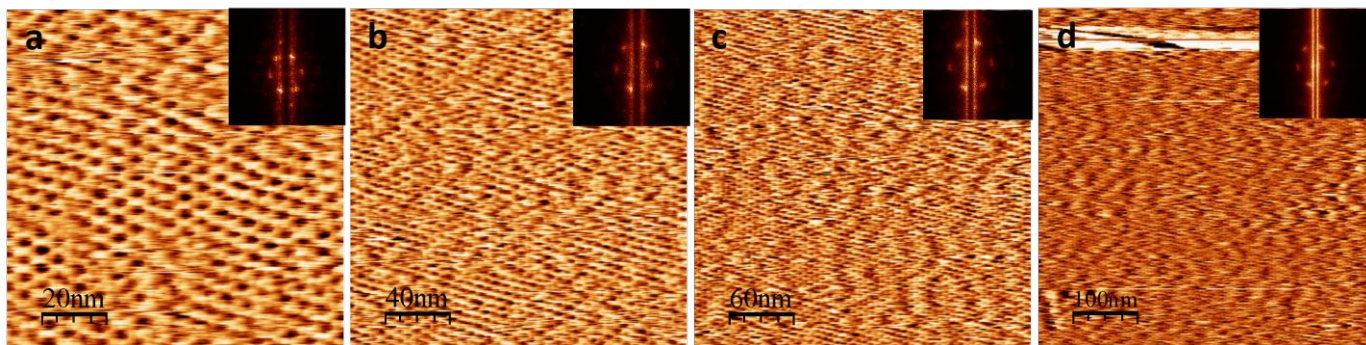
Fig. S2.10 On-surface products of IPA$_{18}$ and pP reaction mixture at 0.1mM. STM images of large single domain from 100×100 nm^2(a), 200×200 nm^2 (b), 300×300 nm^2(c), up to 500×500 nm^2 size (d) with 2D-FFT onset showing a single domain orientation.

On-surface reaction of IPA$_{22}$ + pP : When drop-casting reaction mixture of 0.05 mM onto HOPG, polymer-like lamellae formed on the surface (Fig. S2.11a). Increasing concentration up to 0.1mM also led to formation of similar polymer-like lamellae on the surface, except that the lamellae were not stable when scanning at high current (Fig. S2.11b) and that some small molecular islands formed on top of the polymers (bright flakes in Fig. S2.11b, c). Thus it can be learnt that the lamellae formed by IPA$_4$ is less dependent on the applied concentration as compared to the other IPA$_n$ monomers.
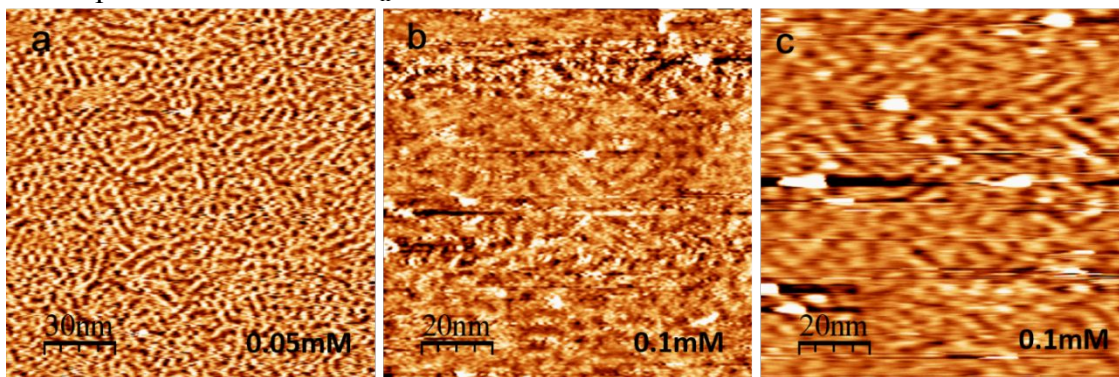

Fig. S2.11 STM images of the on-surface products of IPA$_{22}$ and pP reaction mixture at 0.05 mM (a), at 0.1 mM scanned at high (b) and low current (c).
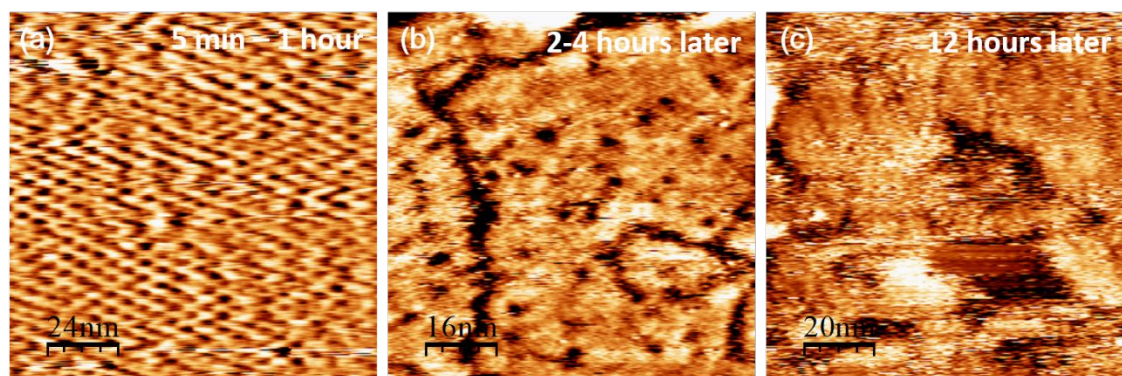
Fig. S2.12 STM images of reaction mixture of IPA$_{18}$ and pP (0.1mM each in TCB with 0.1% octanoic acid as a catalyst) deposited at the HOPG/TCB interface within (a) 5 min – 1 hr, (b) 2-4 hr, and (c) 12 hr.

3. Molecular models of the self-assembly of monomers and oligomers
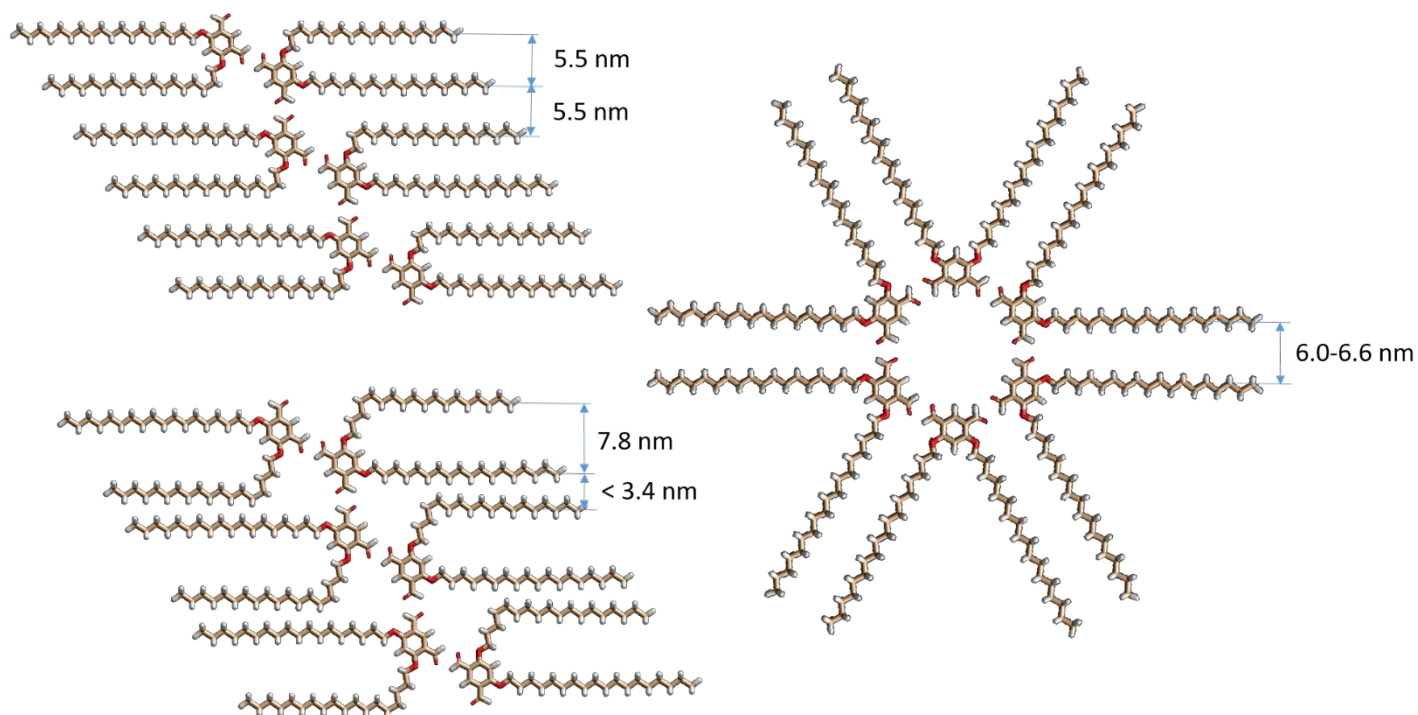
Fig. S3.1 Failed molecular models of the self-assembly of IPA$_{18}$ monomers. The closest inter-chain carbon to carbon distances are either too large (5.5 nm, 6.0-6.6 nm, 7.8 nm) or too small (<3.4 nm) for vdW contacts towards effective alkyl chains interdigitation.
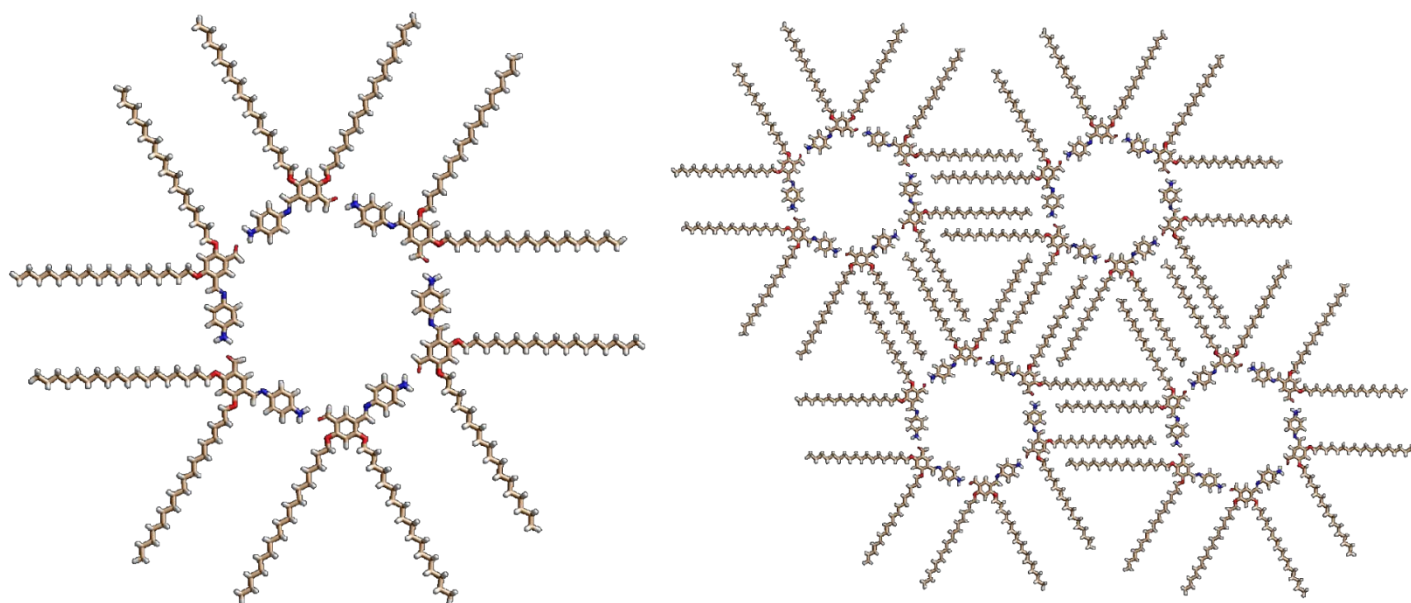
Fig. S3.2 Molecular model of the self-assembly of IPA$_{18}$-pP dimers into the proto-macrocyclic structure and array.

4. Supramolecular structure optimization by MM+

Each type of supramolecular cluster was constructed according to experimentally determined unit cell parameters. The clusters optimized by MM+ force field to a rms deviation of energy gradient smaller than 0.01 kcal/(Å·mol). Following the optimization process, the planarity of the clusters was checked, so as to mimic the on-surface self-assembly. To reduce the computational cost, some parts of the alkyl chains were minimized into methyl groups. In addition, vdW interactions of the interdigitated alkyl chains and their surface adsorption energy were estimated based on the following parameterization and assumptions:

A. Parametrization
- Interactions of the alkyl chains with the HOPG substrate[1]: -64.2 meV/CH_2 (-1.48 kcal/mol)

- Interaction between interdigitated alkyl chains[2]:
1) -49.2 meV/CH_2 (-1.135 kcal/mol) if flanked at both sides by alkyl chains
2) -22 meV/CH_2 (-0.507 kcal/mol) if only flanked by another alkyl chain at one side
Methyl (CH_3) groups are considered as CH_2 groups both in the estimation of adsorbate-substrate and adsorbate-adsorbate interactions.

B. Assumptions/Simplifications
Solvent-molecule and solvent-substrate interactions are not taken into account.
The following aspects are not taken into account:
1) not all alkyl chains are in epitaxy with the graphite substrate;
2) the alkyl chain-alkyl chain interactions are not maximized.
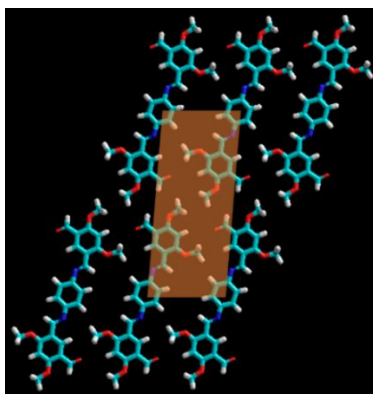
Fig. S4.1 Close-packed trimers model. Unit Cell dimension: a = 2.1 nm, b = 0.9 nm, α = 86°; each UC contains one (IPA_1-pP-IPA_1) trimer.
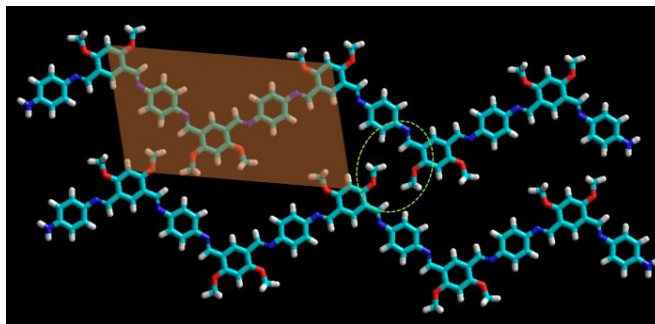
Fig. S4.2 Zigzag polymer lamella model with alkyl chains projecting from the surface. Unit Cell dimension: a = 1.25 nm, b = 2.2 nm, α = 76.5°; each UC contains two (IPA_1-pP) repeating units.

Fig. S4.3 Zigzag polymer lamella model with alkyl chains interdigitated adsorbed on the surface (not optimized). Unit Cell dimension: C_{22}, a = 4.1 nm, b = 2.2 nm, α = 88°; C_{18}, a = 3.6 nm, b = 2.2 nm, α = 88°; C_{16}, a = 3.4 nm, b = 2.2 nm, α = 88°.
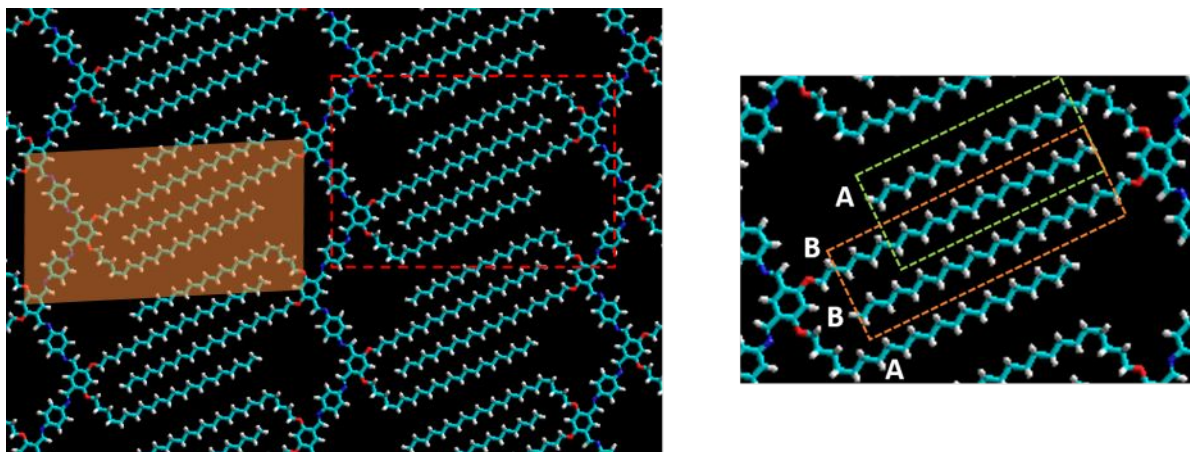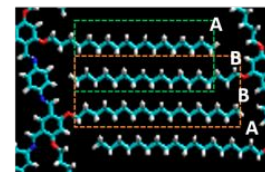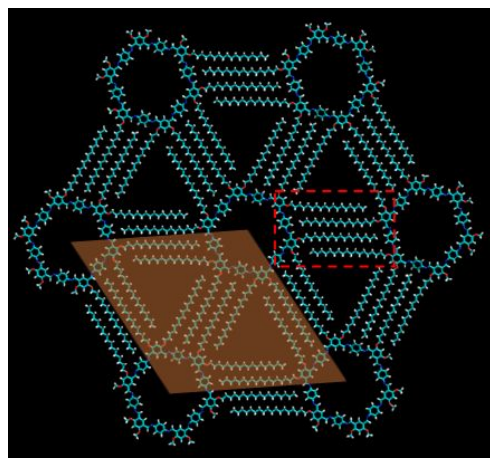
Each UC contains two (IPA$_n$-pP) repeating units (n=22); all CH$_2$ alkyl chains are adsorbed on HOPG surface.

Chain A: (n-6) CH$_2$ are interdigitated on one side, where n denotes the number of carbons in each R-chain;

Chain B: (n-6) CH$_2$ are interdigitated on both sides, and 3 CH$_2$ are interdigitated on one side.

(a)

(b)
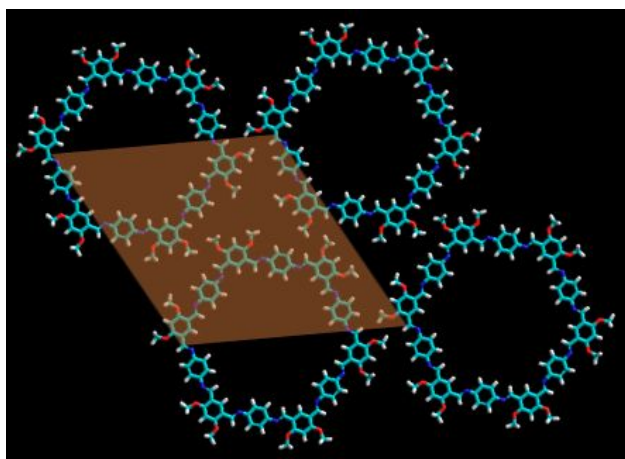
Fig. S4.4 Macrocycle network model:

(a) Unit Cell dimension: a = b = 3.34 nm, α = 60°; each UC contains one (IPA$_1$-pP)$_6$ macrocycle.

(b) Unit Cell dimension: a = b = 3.34 + 0.12 (n-1) nm, α = 60°; each UC contains one (IPA$_n$-pP)$_6$ macrocycle (n=18)

All CH$_2$ alkyl chains are adsorbed on HOPG surface.

Chain A: (n-3) CH$_2$ are interdigitated on one side;

Chain B: (n-3) CH$_2$ are interdigitated on both sides, and 3 CH$_2$ is interdigitated on one side.

5. MM+ calculations of surface adsorption energy

The molecule of interest was placed on a (larger) graphene cluster and optimized by MM+ force field to a rms deviation of energy gradient smaller than 0.01 kcal/(Å·mol). The H-terminated graphene cluster was kept frozen during the optimization process.

The adsorption energy is obtained as:

$$E_{ads} = E_{(molecule + HOPG)} - E_{HOPG} - E_{molecule}$$

(a)　　　　　　　　　　　　　　　　　　　　**(b)**
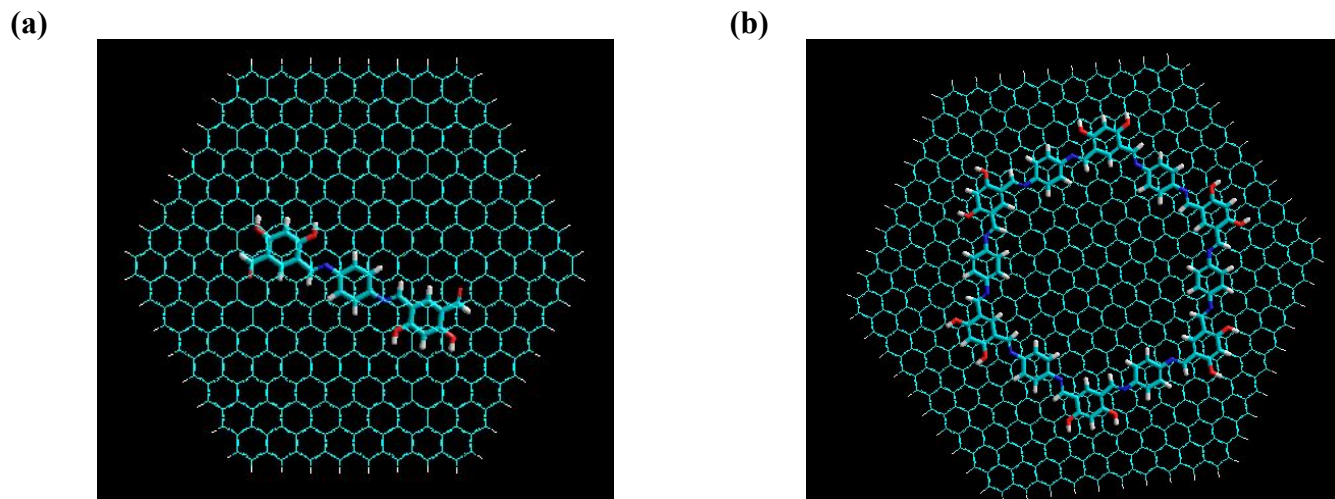
Fig. S5.1 (a) Configuration used for calculation of the adsorption energy of (IPA-pP-IPA) trimer on HOPG surface, **(b)** Configuration used for the calculation of the adsorption energy of (IPA-pP)$_6$ macrocycle on HOPG surface.

Linear polymer adsorption on HOPG surface

The adsorption energy for polymeric unit is obtained as:

$$E_{abs}(\text{polymeric unit}) = 1/2[(E_{2,ads} - E_{1,ads}) + (E_{3,abs} - E_{2,ads})]$$

(a)　　　　　　　　　**(b)**　　　　　　　　　**(c)**
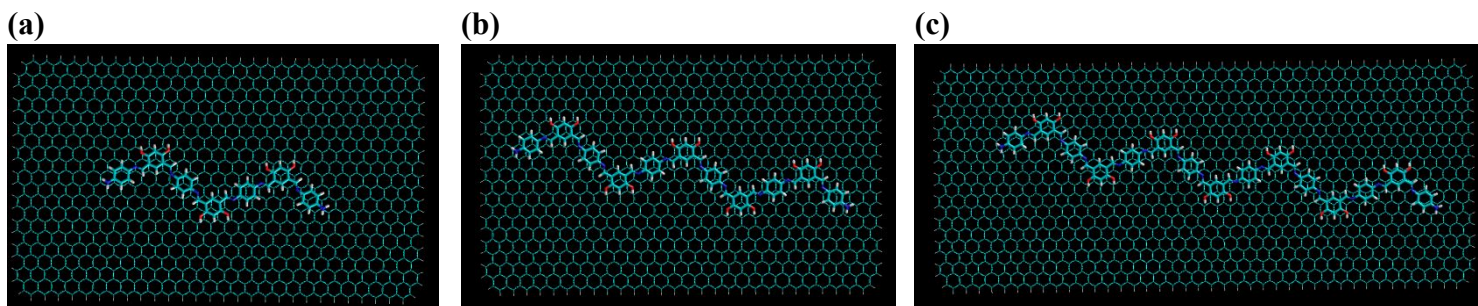
Fig. S5.2 Configurations used for the calculation of the adsorption energy of linear polymers on HOPG surface. Equilibrium energies for (a), (b) and (c) are $E_{1,ads}$, $E_{2,ads}$, $E_{3,ads}$, respectively.

6. DFT calculations of molecular strain

DFT calculations were performed with Gaussian 0B3LYP functional with the 6-31G(d) basis set. Calculations were done on isolated molecules or molecular dimers, being optimized in gas phase. To reduce the computational cost, the alkyl chain lenght was limited to methyl groups, which would still contain similar steric (if there is any) between the alkoxy chain and aromatic backbones.

(a)

(b)

(c)
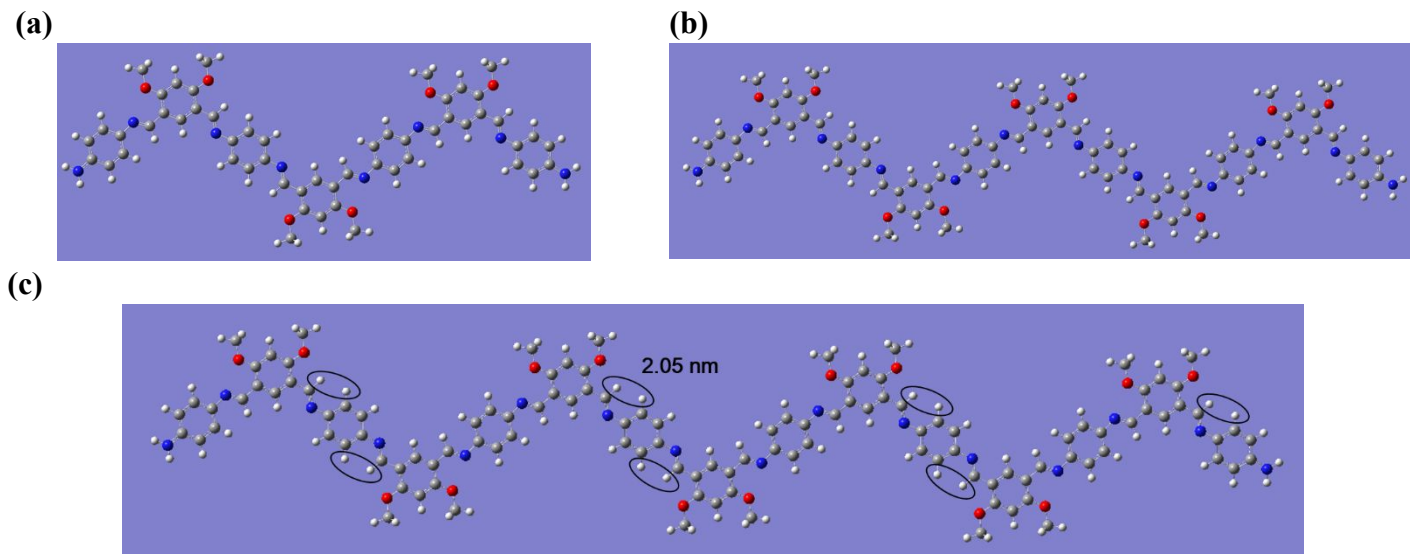
Fig. S6.1 DFT optimized structures of oligomers at B3LYP/6-31G(d). Equilibrium energies for (a), (b), (c) are E_1, E_2, E_3, respectively.

The energy per polymeric unit is obtained as: $E_{polymeric\ unit} = 1/2\ [(E_2-E_1) + (E_3-E_2)]$
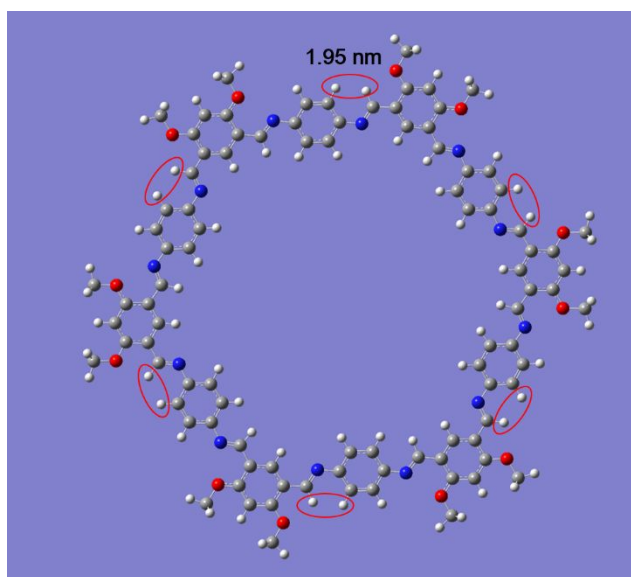
Fig. S6.2 DFT optimized structure of the macrocycle[6+6] at B3LYP/6-31G(d) with equilibrium energy $E_{macrocycle}$

The molecular strain is calculated as: $\Delta E_{strain} = E_{macrocycle} - 3E_{polymeric\ unit}$

The ring strain is mostly due to the steric hindrance between the much closer protons of imine and phenyl ring (d = 1.95 nm, red ovals in Fig. S6.2) than that of open-chain polymers (d = 2.05 nm, black ovals in Fig. S6.1c).

DFT calculation of methoxy unit interaction at B3LYP/6-31G(d)

(a)

(b)
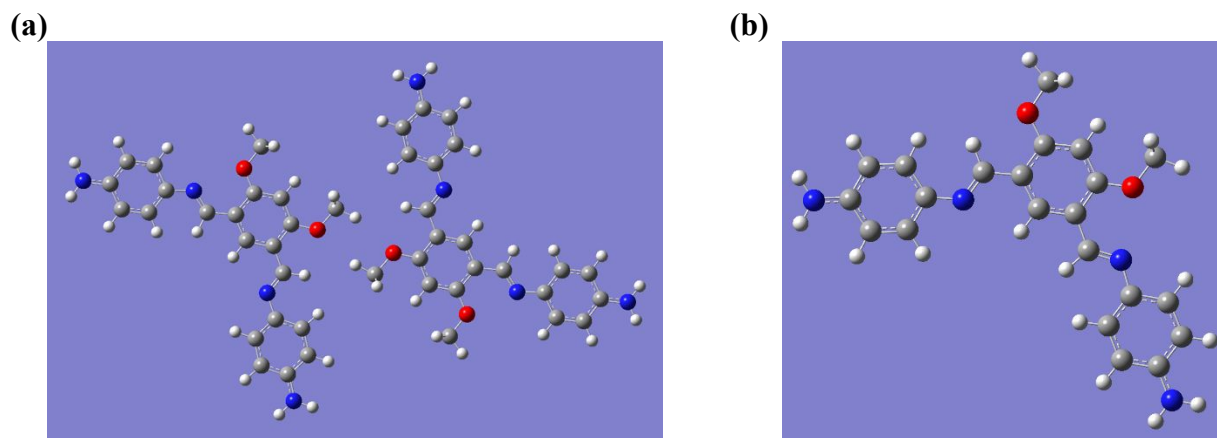
Fig. S6.3 DFT optimized structures of oligomers at B3LYP/6-31G(d). Equilibrium energies for (a) and (b) are respectively E_{dimer} and $E_{monomer}$

The methoxy unit interaction is obtained as: $E_{interaction} = E_{dimer} - 2E_{monomer}$, which has been applied to the following supramolecular structures:

(a)

(b)
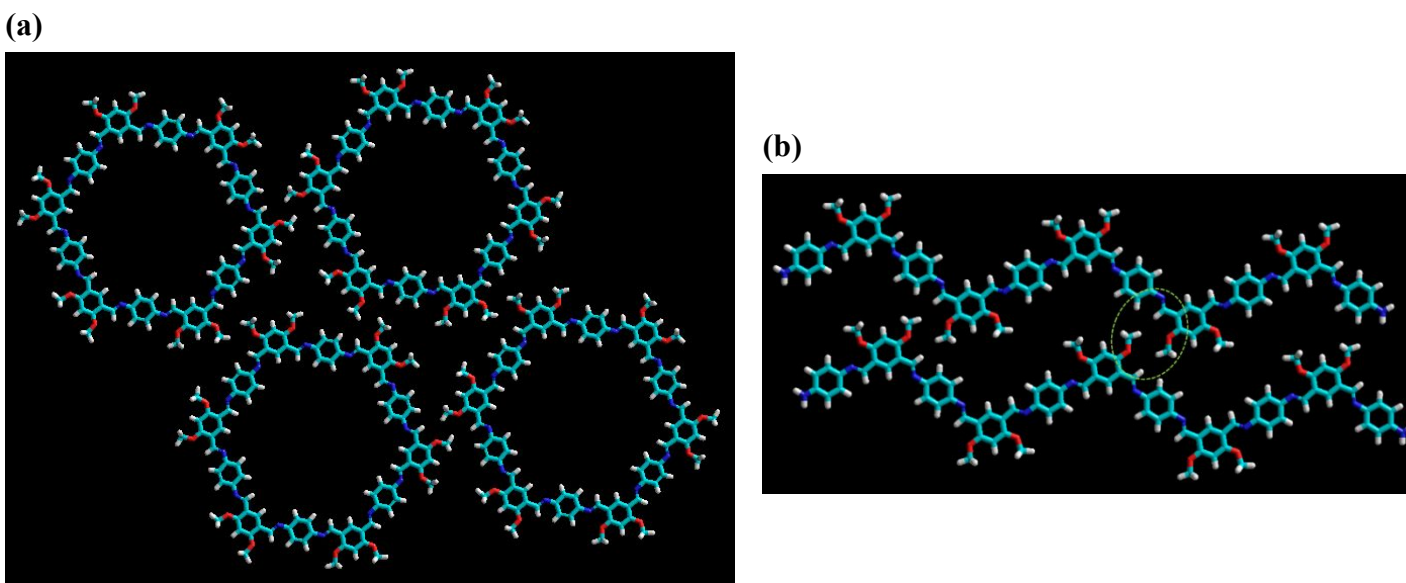
Fig. S6.4 Macrocycle honeycomb (a) and close packed linear polymer (b) structures

Generation of total enthalpy/energy w.r.t. the number of carbon in alkoxy chains

$E_{tot} = E_{vdW} + E_{abs} + E_{strain}$, which is normalized by the area A per unit cell as E_{tot}/A.

To avoid any odd-even effect and to match our actual experimentally used molecular building blocks, only supramolecular systems including IPA_n monomers with an even number of carbons n were considered.

7. Additional Plots

Fig. S7.1 Packing density of the three supramolecular systems by atom per unit cell area.

Fig. S7.2 Size comparison between macrocycle cavities B and A, as defined in Fig. 3 in the manuscript.

8. Combined DFT and MM+ of TCB solvent co-adsorption in macrocycle networks

In the modeling of TCB co-adsorption in the macrocycle networks, gas phase DFT (B3LYP/6-31G(d) functional) was first applied to predict all possible TCB cl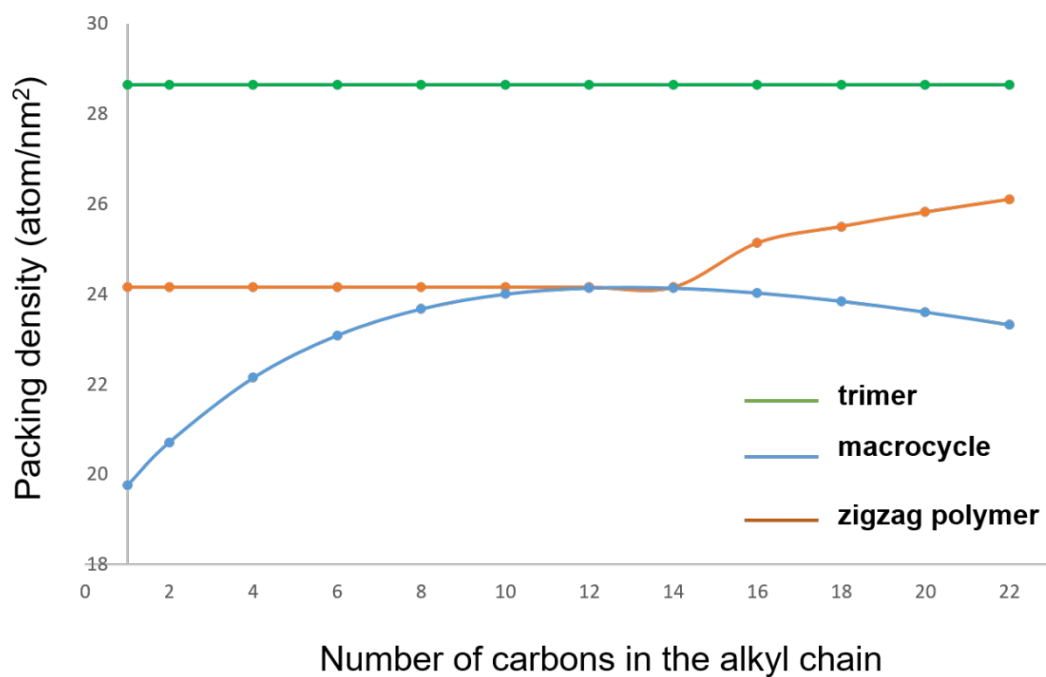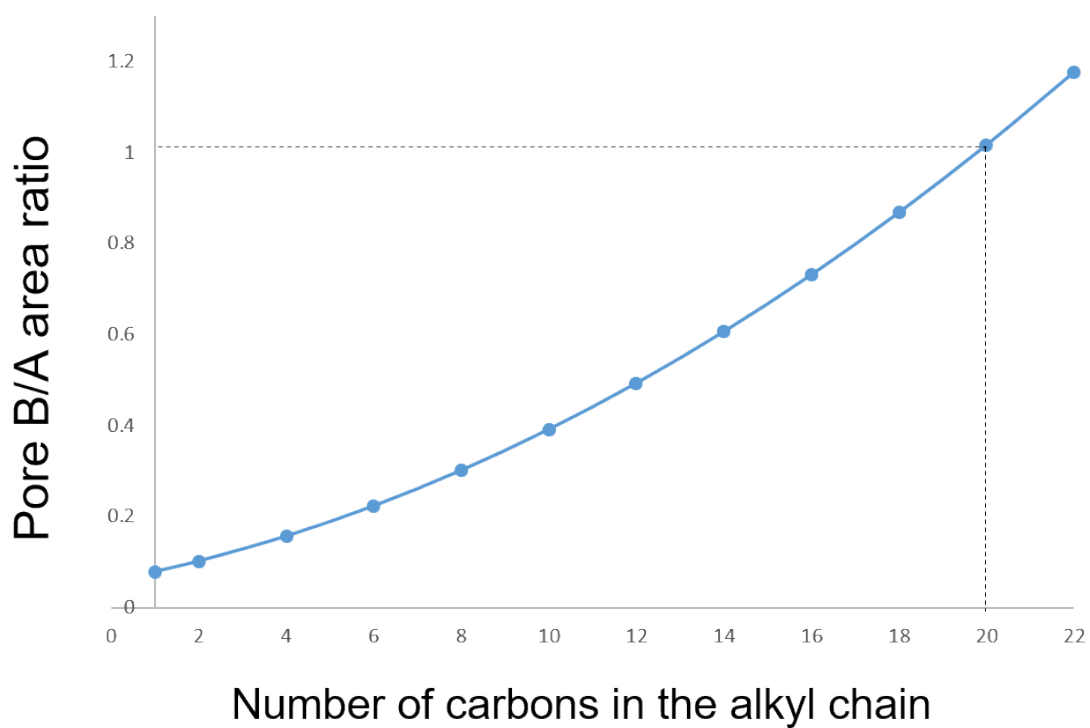usters constrained in plane. All possible TCB clusters converged in DFT calculations are summarized in Fig. S8.1. Assuming the pore spaces are occupied by the maximum numbers of TCB molecules, the structures of TCB molecules in the pores were optimized using the following steps. For the hexagonal pore A, we modeled with different numbers of co-adsorbed TCB molecules (three, four and six molecules) with lateral rotation of TCB clusters to favor C-H···Cl-C interaction. Three is found the maximum number of TCB molecules that can fit in pore A (Fig. S8.2). Then, 3 macrocycles of each MM+ optimized [IPA$_n$-pP]$_6$ honeycomb structure (Fig. S8.3) were placed on graphene for further MM+ optimization to remove slight the ring torsion (see 1st panel in Fig. S8.4). After MM+ optimization, the 3 alkyl chains at the rim of the trigonal pore B were extracted and TCB molecules are placed in the pore for DFT (M06-2X/6-31G(d) functional) optimization (Fig. S8.4). TCB co-adsorption in [IPA$_n$-pP] macrocycle networks is summarized in Fig. S8.5. The additional stabilization energy contributed by TCB co-adsorption has been tabulated in Table S8.1.

TCB hexamers   **TCB tetramers**   **TCB trimers**   **TCB dimers**
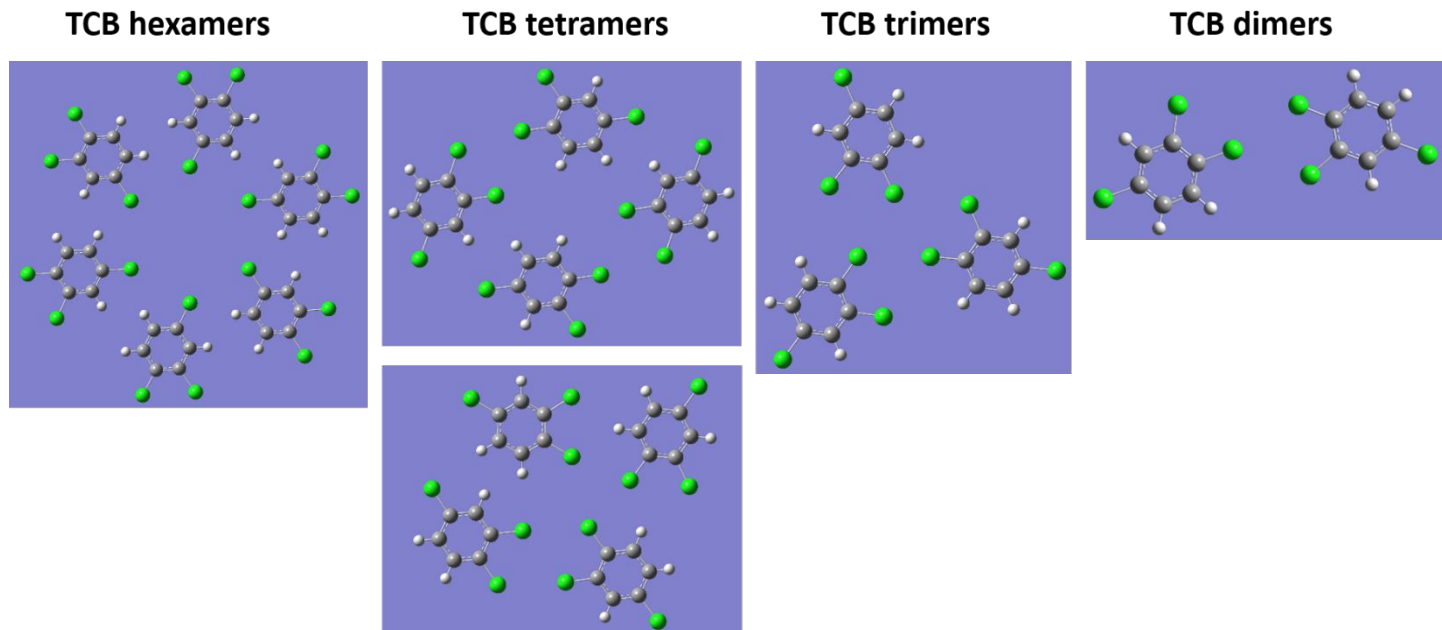
Fig. S8.1 Gas-phase DFT optimized TCB clusters by M06-2X functional at 6-31G(d) basis set.

DFT optimization by M06-2X/6-31G(d)

Space-filling models of TCB clusters failed to fit in the macrocycle pore:
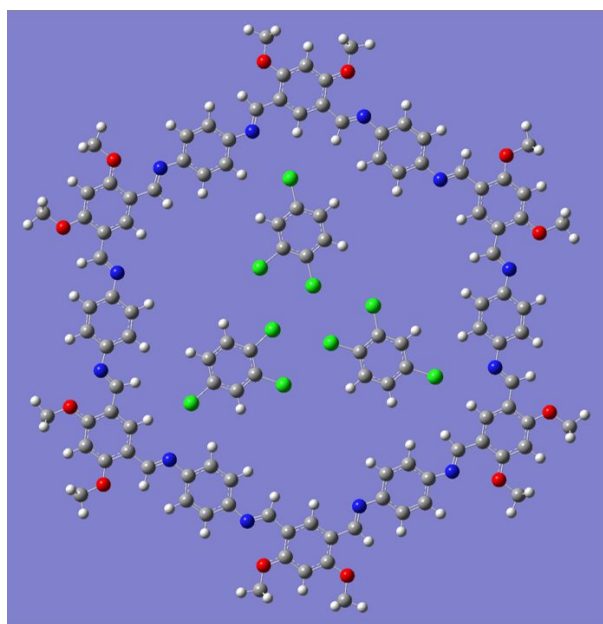
TCB hexamer

Side view (symmetry "C6h" imposed)
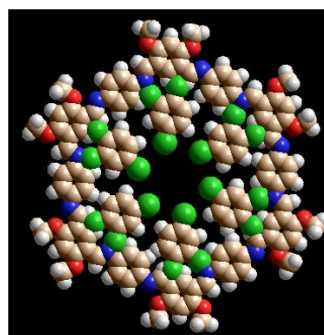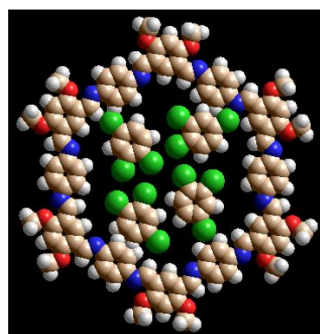
TCB tetramer   **TCB tetramer**
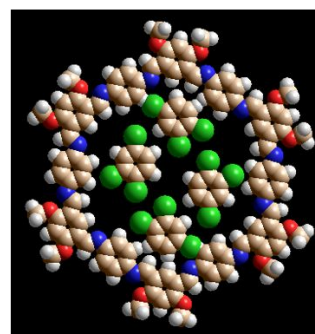
Fig. S8.2 TCB cluster in macrocycle pore optimized by DFT calculations (left panel), and space-filling models that TCB clusters failed to fit inside (right panel).

[IPA$_{10}$-pP]$_6$ [IPA$_{12}$-pP]$_6$ [IPA$_{14}$-pP]$_6$

[IPA$_{16}$-pP]$_6$ [IPA$_{18}$-pP]$_6$ [IPA$_{20}$-pP]$_6$ [IPA$_{22}$-pP]$_6$
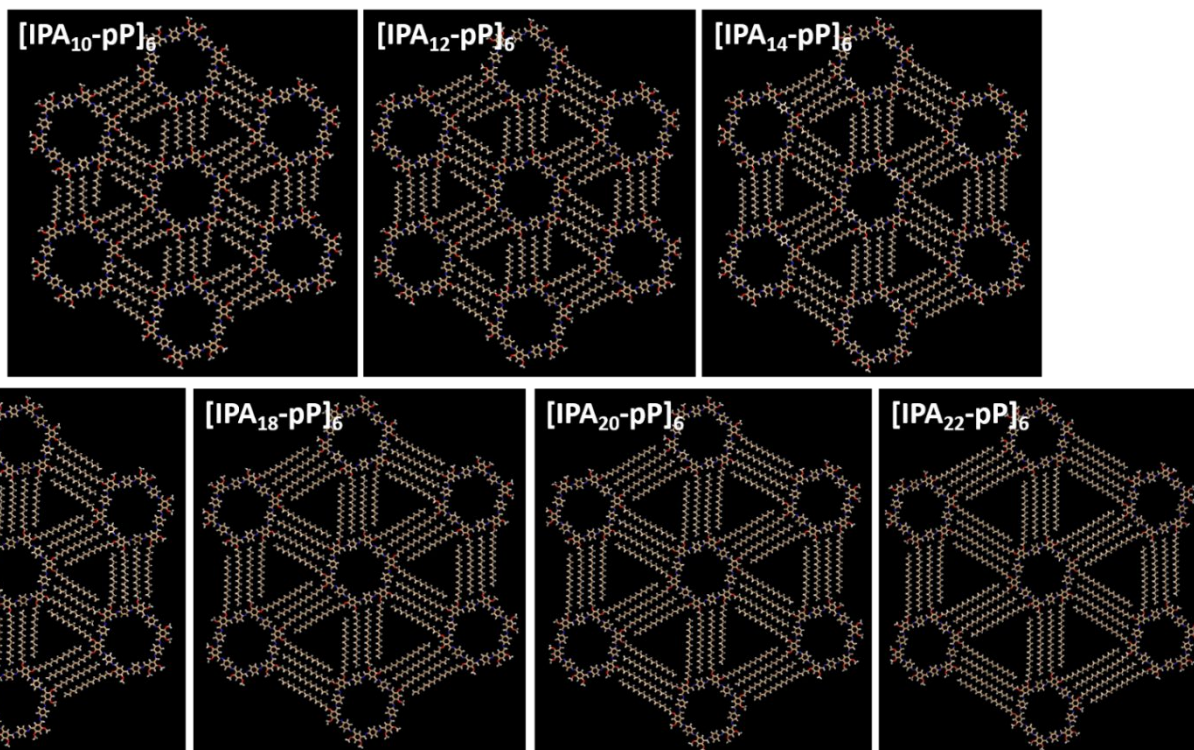
Fig. S8.3 Optimized [IPA$_n$-pP]$_6$ macrocycle supramolecular structures by MM+ simulations with RMS < 0.01 kcal/(Å·mol). The alkyl side chains at the edge of the supramolecular structures were shortened to methyl group for simplicity.
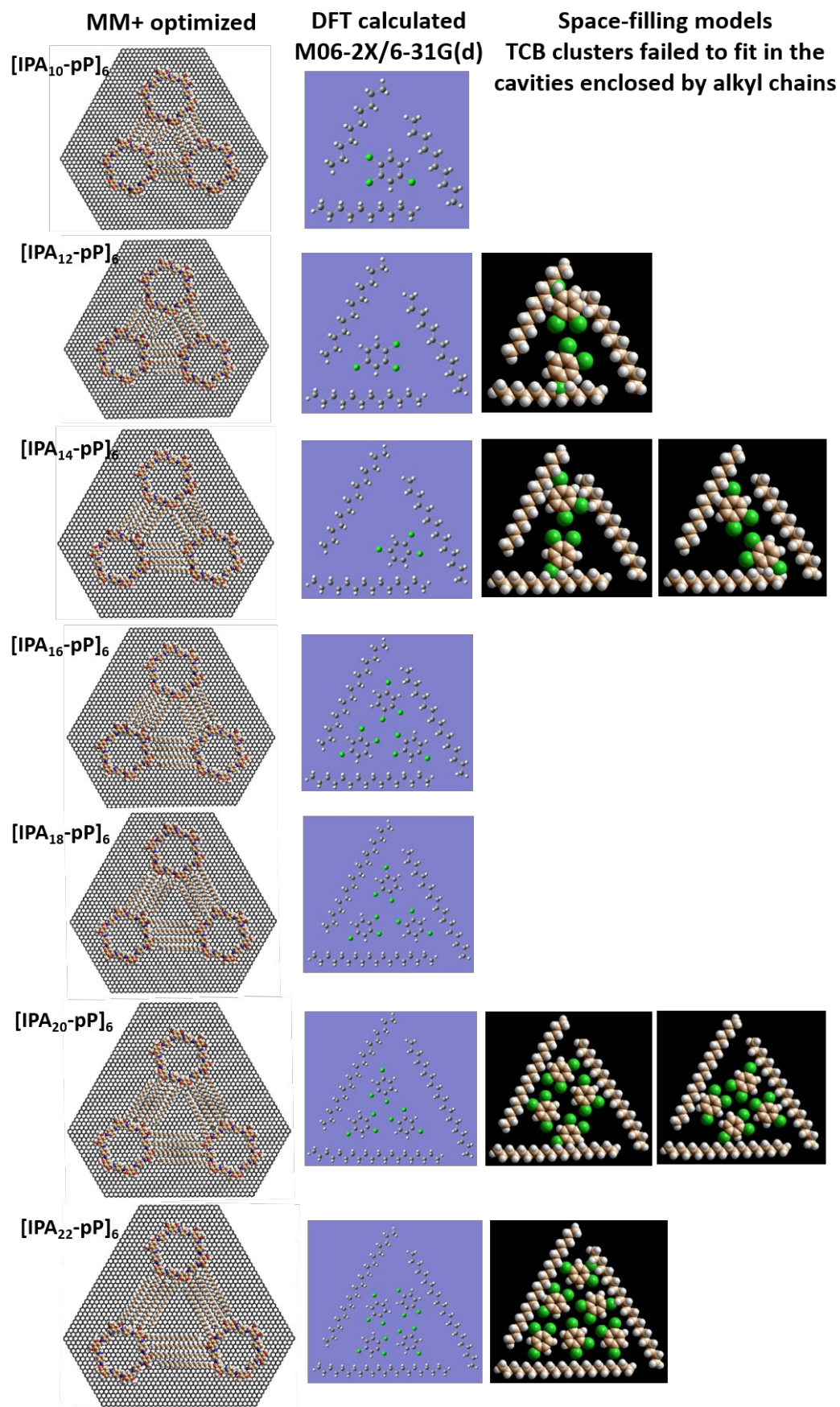
Fig. S8.4 Co-adsorbed TCB clusters in triangle pore enclosed by alkyl chains optimized by DFT calculations and space-filling models showing the TCB clusters that failed to fit in the cavities.
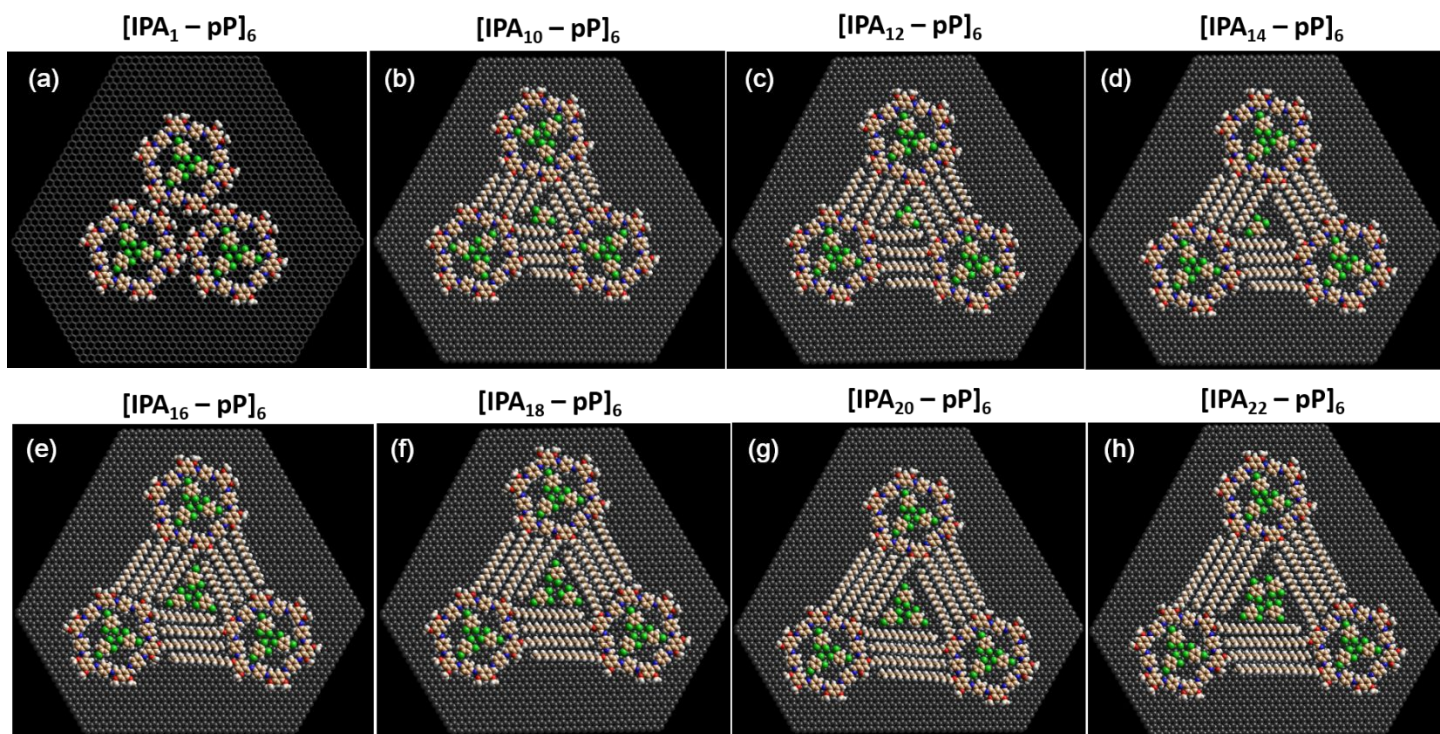
Fig. S8.5 Molecular modeling of the co-adsorbed TCB solvent molecules in the macrocycle networks of (a) [IPA$_1$-pP]$_6$ (b) [IPA$_{10}$-pP]$_6$, (c) [IPA$_{12}$-pP]$_6$, (d) [IPA$_{14}$-pP]$_6$, (e) [IPA$_{16}$-pP]$_6$, (f) [IPA$_{18}$-pP]$_6$, (g) [IPA$_{20}$-pP]$_6$, and (h) [IPA$_{22}$-pP]$_6$. TCB co-adsorption of macrocycles of alkyl chains shorter than C$_{10}$ can be referred to the model (a).

Table S8.1 A summary of additional stabilization energy from TCB co-adsorption in the macrocycle networks.

Macrocycle networks	# TCB in 1 macrocycle, 2 alkyl chain enclosed cavities per unit cell	E_{inter} (TCB co-adsorption)[a] kcal/mol/unit cell	Area $_{unit\ cell}$ nm^2	E_{inter} (TCB co-adsorption) kcal/mol/nm^2
[IPA$_1$-pP]$_6$	3×1, 0×2	-2.32	9.72	-0.239
[IPA$_2$-pP]$_6$	3×1, 0×2	-2.32	10.4	-0.223
[IPA$_4$-pP]$_6$	3×1, 0×2	-2.32	11.9	-0.195
[IPA$_6$-pP]$_6$	3×1, 0×2	-2.32	13.5	-0.172
[IPA$_8$-pP]$_6$	3×1, 0×2	-2.32	15.2	-0.153
[IPA$_{10}$-pP]$_6$	3×1, 1×2	-7.31	17.0	-0.430
[IPA$_{12}$-pP]$_6$	3×1, 1×2	-7.66	18.9	-0.406
[IPA$_{14}$-pP]$_6$	3×1, 1×2	-8.36	20.9	-0.400
[IPA$_{16}$-pP]$_6$	3×1, 3×2	-14.27	23.0	-0.621
[IPA$_{18}$-pP]$_6$	3×1, 3×2	-14.47	25.2	-0.575
[IPA$_{20}$-pP]$_6$	3×1, 3×2	-9.02	27.5	-0.328
[IPA$_{22}$-pP]$_6$	3×1, 4×2	-10.91	29.8	-0.366

a. E_{inter} (TCB co-adsorption per unit cell) = ½ × {[E_{tot} (macrocycle+3 TCB) – E_{tot} (macrocycle) – E_{tot} (3 TCB)] + 2 × [E_{tot} (3 alkyl chains + n TCB) – E_{tot} (3 alkyl chains) – E_{tot} (n TCB)]}, n is the number of TCB fitted in the intermolecular cavities enclosed by the interdigitated alkyl chains. The Etot are obtained from DFT calculations by M06-2X functional at 6-31G(d) basis set.

9. Molecular Dynamics Simulation of molecular adsorption at the solvent/graphite interface

MD simulations of graphite/reactant/TCB systems were run with 3D periodic boundary conditions, at constant volume and T=300 K, with all boxes containing a horizontal slab of four graphite layers, thick enough to mimic the bulk for the chosen Lennard-Jones cutoff (graphite atoms are charge-less), sizing 60.4 Å by 59.556 Å. The vertical position of graphite atoms was kept fixed at the experimental (initial) X-ray geometry[3] using a harmonic constraint with constant 5 kcal/mol/ Å². For simulations in vacuum the vertical (normal to the graphite slab) box size was set to 200 Å, while for simulations in TCB, a thickness of about 102-105 Å was necessary to accommodate 1500 solvent molecules, upon previous equilibration at p=1 atm. All samples contained also one target molecule or oligomer (pP, IPA_1, IPA_8, IPA_{12}, IPA_{18}, $pP-IPA_1$, $pP-IPA_4$, $IPA_1-pP-IPA_1$, $IPA_4-pP-IPA_4$), for which the free energy of adsorption as a function of the distance from the first graphite layer was evaluated with the adaptive biasing force scheme.[4] In vacuum, 20 nanoseconds can be sufficient to obtain a smooth free energy profiles, while in TCB typical runs are one order of magnitude longer, with the required simulation time increasing with the length of the IPA alkyl chain.
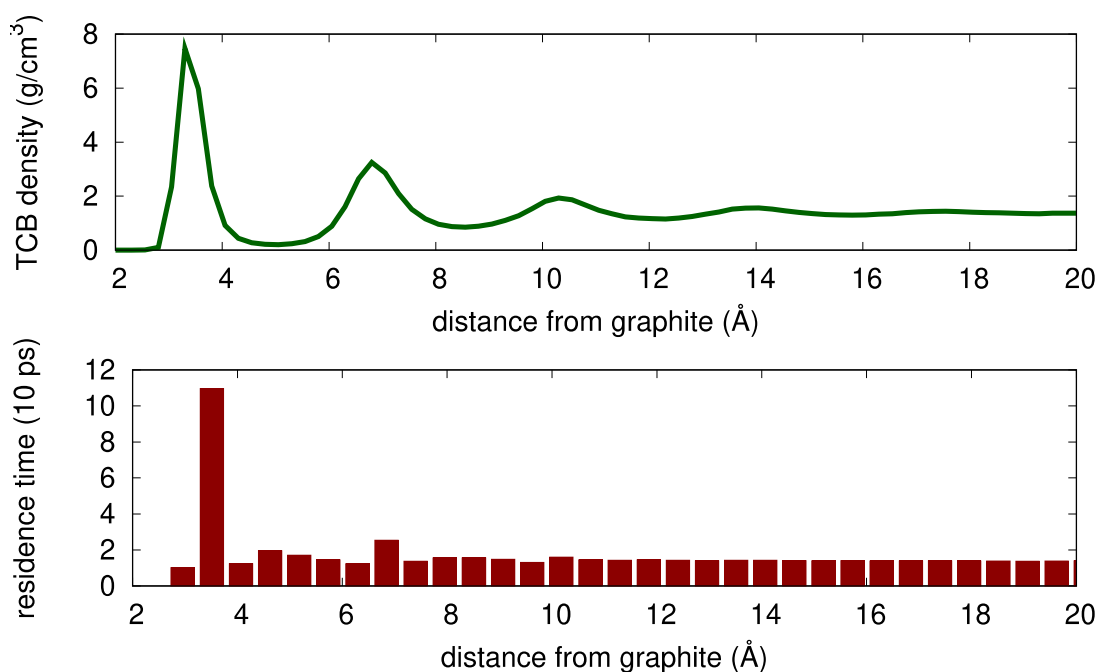
Fig. S9.1 Density and surface retention time of TCB molecules as a function of the distance from the graphite surface, calculated for horizontal slices of the 0.5 Å-thick samples. **Top panel**: the solvent is highly structured with at least three solvation layers at the interface with graphite. Based on the height of the density peaks and the width of the density oscillation, only the first TCB layer should present a solid like positional order (also highlighted by the snapshots in Fig. 4b). **Bottom panel**: by measuring the retention time of solvent molecules in horizontal slices of the samples at increasing distance from the surface, the dynamics of the first solvation layer is indeed slowed down about five times with respect to the bulk, but is not blocked, so the layers retain a fluid-like nature. The retention time decreases for the second solvation layer (peak at 6.5-7 Å), while moving further away from graphite the distance dependence fades away.

The free energies of adsorption listed in Fig. S9.2 and Table. S9.1 are calculated as follows:

Referring to the absorption free energy profiles illustrated in Fig. S9.3, at short distances (< 3 Å), close to the graphite layers, a repulsive profile is invariably found, immediately followed by a minimum whose position shifts at higher distances for bulkier molecules. Then, at least in vacuum (Fig. S9.3, left panel), the energy rises at increasing distance, until reaching a plateau. At these distances, the molecule does not feel anymore the attraction (van der Waals) potential of the graphite surface. Hence, the free energies of adsorption are the difference from the plateau value and the value at the minimum close to the graphite, conventionally set as the zero of the energy scale, and positive if the adsorption is thermodynamically favored.
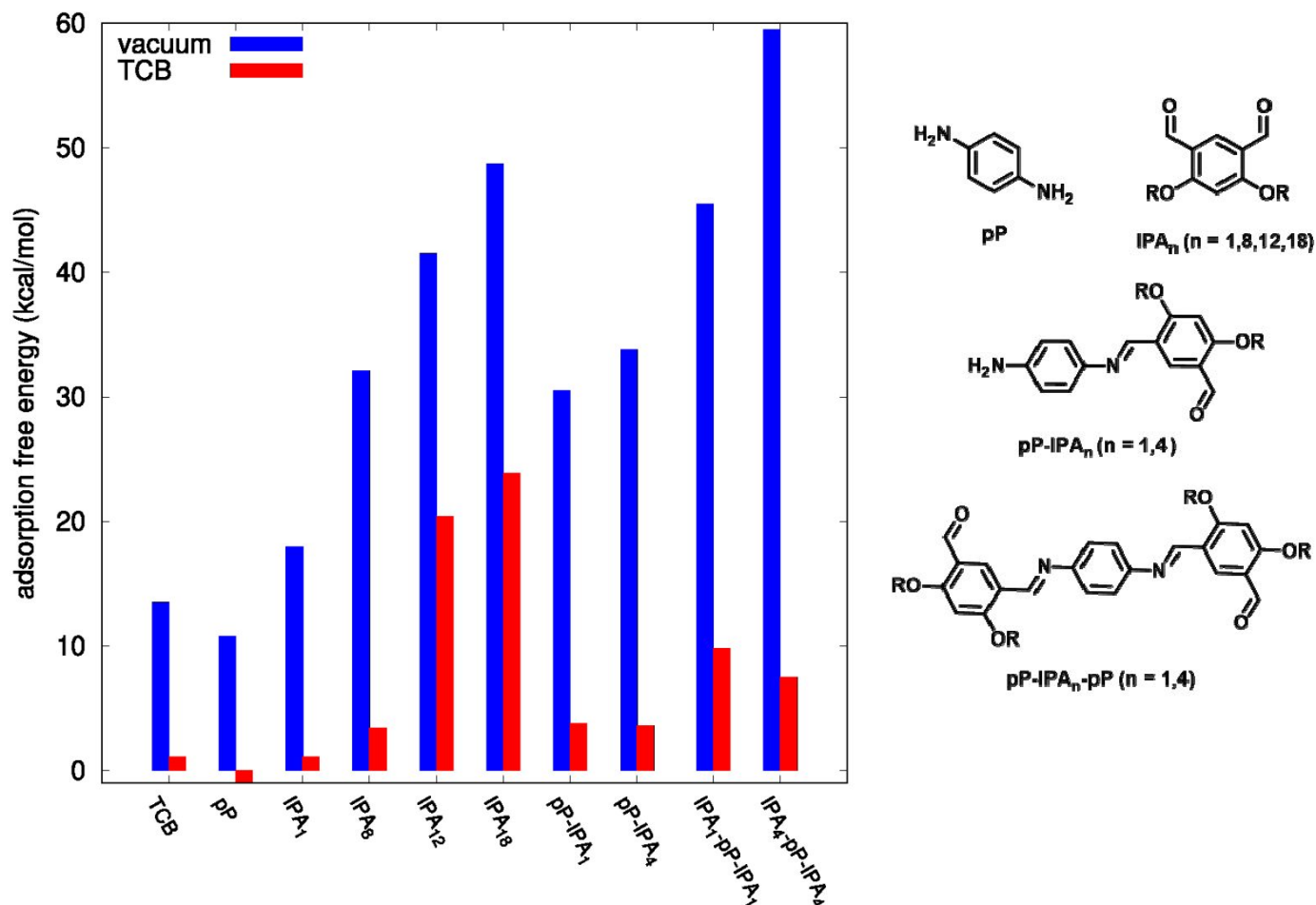
Fig. S9.2 Comparison of absorption energy on graphite in vacuum and TCB for selected monomers. The adsorption free energies in vacuum (**blue bars**) are approximately proportional to the molecular size of the adsorbed species, while in TCB, the adsorption free energies (**red bars**) of monomers and dimers with short alkyl chains are negligible as compared to that of TCB solvent. The driving force appears to be the interactions between the long alkyl chains on IPA units with graphite, and the aromatic moieties prefer the solvent to the substrate. This adsorption preference finds an experimental confirmation from the observation of dotriacontane in concentrated 1-phenyloctane forming ordered layers on HOPG.[5] The error bars of the predicted free energies are estimated around 10% or a few kcal/mol, including several possible sources of errors: 1. the convergence of the free energy calculation, 2. the cutoff used for Lennard-Jones interaction by applying empirical force field parameters, and 3. the limited thickness and unrealistic regularity of the graphite surface.
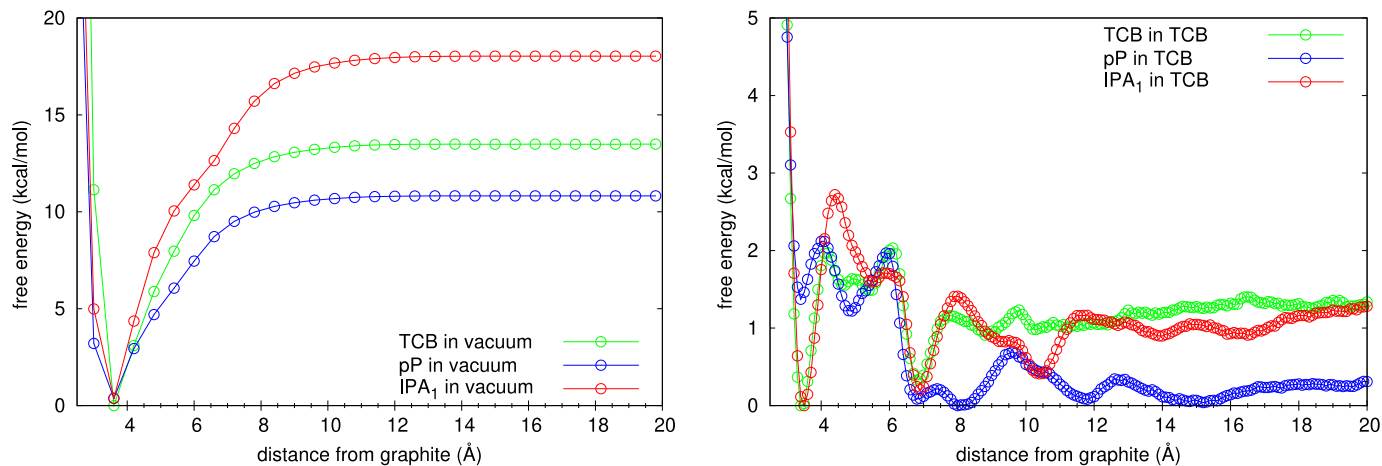
Fig. S9.3 Adsorption free energy profiles of monomers and solvent in vacuum and TCB solvent, as a function of the distance between their center of mass and the atoms of in the first graphite sheet. **Left panel**: In vacuum, both monomers pP and IPA$_1$ and solvent TCB possess adsorption energies at the order of 10 kcal/mol. **Right panel**: In TCB, the energy values at the plateau are only slightly higher than the minimum at the surface, and small barriers separate the two regions, with maxima in correspondence of the higher density peak of the solvent layer in Fig. S9.1. The adsorption free energy of pP is lower in bulk solution with respect to the surface, and consequently, it is very unlikely to participate in surface reactions, also considering that, on the contrary, the adsorption of TCB solvent molecules is thermodynamically favored.

Table S9.1 A summary of key parameters of the adsorption of monomers and oligomers at the TCB/graphite interface derived from MD simulation. Retention time is estimated as A * exp[E_A/(RT)], where A = 10^{-12} s, and E_A is the adsorption free energy on graphite surface in TCB.

Adsorbed species	E_A, vacuum (kcal/mol)	E_A, TCB (kcal/mol)	Surface Retention Time (s), TCB, 298.15 K	Min conc. for full surface coverage (1× 1 cm^2)
TCB	13.5	1.1	6×10^{-12}	n/a
pP	10.8	-1.4	1×10^{-13}	n/a
IPA$_1$	18.0	1.1	6×10^{-12}	n/a
IPA$_8$	32.1	3.4	3×10^{-10}	n/a
IPA$_{12}$	41.5	20.4	6×10^2	For pP-IPA$_{12}$, 9.0×10^{-6} M
IPA$_{18}$	48.7	23.9	2×10^5	For pP-IPA$_{18}$, 6.8×10^{-6} M
pP-IPA$_1$	30.5	3.8	6×10^{-10}	n/a
pP-IPA$_4$	33.8	3.6	4×10^{-10}	n/a
IPA$_1$-pP- IPA$_1$	45.5	9.8	1×10^{-5}	9.2×10^{-5} M
IPA$_4$-pP- IPA$_4$	59.5	7.5	3×10^{-7}	Refer to IPA$_1$-pP-IPA$_1$[a]

[a] Experimentally, pP-IPA$_4$-pP is observed to assemble on the surface in the same fashion as pP-IPA$_1$-pP, i.e. the alkyl chains are desorbed from the surface. Therefore, we assume that pP-IPA$_4$-pP adopts the same adsorption energy as pP-IPA$_1$-pP.

10. Synthesis of IPA$_n$ compounds and their precursors

^{1}H- and ^{13}C-NMR-spectra were recorded with Varian Mercury 300 Plus 300 MHz NMR with 2-channel broadband Mercury Plus console, Varian 300 H/F/X PFG tunable probe and VNMRJ workstation. Chemical shifts are reported in ppm proportional to the Me$_4$Si-signal. Melting points were determined with the stuart melting point apparatus SMP20 in open capillaries and not corrected.

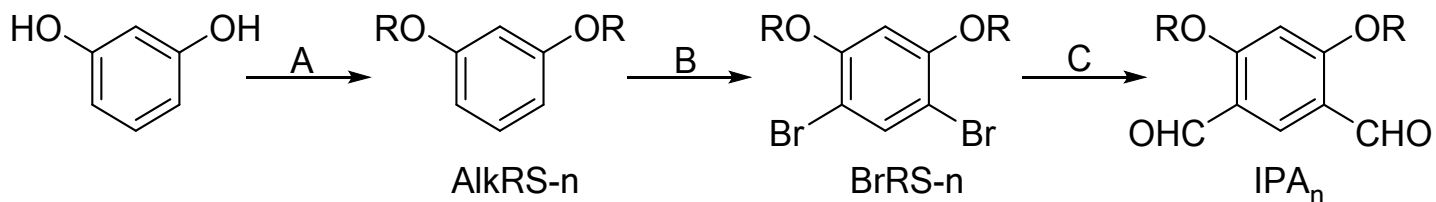General procedures for the preparation of all resorcinol derivatives.

Fig. S10.1 Reaction scheme of the preparation of substituted resorcinols.

A) Bis-Alkylation
To a solution of resorcinol (3.85 g, 34.9 mmol) in 150 mL of argon-purged DMF, 2eq of corresponding alkyl bromide, potassium carbonate (12.24 g, 88.5 mmol) and potassium iodide (1.24 g, 7.5 mmol) were added while stirring. The solution was stirred at 55 °C for 3 days. The mixture was then allowed to cool to room temperature and 150 mL of distilled water added. The formed brown solid was separated by filtration and washed with hot acetone. The products were purified by column chromatography (PE/CH$_2$Cl$_2$ 1:1, v/v, yields ≥ 95 %).

^{1}**H NMR**,^{13}**C NMR** spectra and melting points of the bis(alkylated) products:

AlkRS-1. Commercial

AlkRS-4. Corresponding to the literature[6]

AlkRS-8. Corresponding to the literature[7]

AlkRS-12. Corresponding to the literature[8]

AlkRS-18. ^{1}**H-NMR** (300 MHz, CDCl$_3$): δ(ppm) = 7.13 (t, 1H, J = 7.8 Hz, Ar-H), 6.49 (s, 1H, Ar-H), 6.47 (d, 2H, J = 7.8 Hz, Ar-H), 3.92 (t, 4H, J = 6.6 Hz, –OCH_2–), 1.82-1.71 (m, 4H, –OCH$_2$CH_2–), 1.48-1.22 (m, 60H, –CH_2–), 0.87 (t, 6H, J = 6.6 Hz, –CH$_2$CH_3). ^{13}**C-NMR** (75 MHz, CDCl$_3$): δ(ppm) = 160.4, 129.7, 106.4, 101.4, 67.9, 31.9, 29.7-29.6, 29.4, 29.3, 29.2, 26.0, 22.7, 14.2. **Mp** = 80 – 83 °C.

AlkRS-22. ^{1}**H-NMR** (300 MHz, CDCl$_3$): δ(ppm) = 7.14 (t, 1H, J = 8.0 Hz, Ar-H), 6.50-6.44 (m, 3H, Ar-H), 3.93 (t, 4H, J = 6.7 Hz, –OCH_2–), 1.82-1.71 (m, 4H, –OCH$_2$CH_2–), 1.49-1.21 (m, 76H, –CH_2–), 0.88 (m, 6H, –CH$_2$CH_3). ^{13}**C-NMR** (75 MHz, CDCl$_3$): δ(ppm) = 160.4, 129.7, 106.6, 101.4, 68.0, 31.9, 29.7-29.6, 29.4, 29.3, 29.2, 26.1, 22.7, 14.1. **Mp** = 83 – 86 °C.

B) Bis-Bromination
The alkylated product was dissolved in CH$_2$Cl$_2$ and 2eq of N–bromosuccinimide was slowly added while the solution was stirred at room temperature. The solution was stirred for 2 days and then concentrated under reduced pressure. The residue was washed with methanol, which gave rise to the desired product (yields around 80%) which was collected by filtration.

¹H NMR,¹³C NMR spectra and melting points of the bis(brominated) products:

BrRS-1. Corresponding to the literature[9]

BrRS-4. ¹H-NMR (300 MHz, CDCl₃): δ(ppm) = 7.63 (s, 1H, Ar-*H*), 6.46 (s, 1H, Ar-*H*), 3.99 (t, 4H, *J* = 6.4 Hz, –OC*H₂*–), 1.87-1.75 (m, 4H, –OCH₂C*H₂*–), 1.60-1.46 (m, 4H, –C*H₂*CH₃), 0.99 (t, 6H, *J* = 7.4 Hz, –CH₂C*H₃*). **¹³C-NMR** (75 MHz, CDCl₃): δ(ppm) = 155.6, 135.7, 102.9, 99.8, 69.3, 31.1, 19.2, 13.8. **Mp** = 78 – 81 °C.

BrRS-8. ¹H-NMR (300 MHz, CDCl₃): δ(ppm) = 7.63 (s, 1H, Ar-*H*), 6.46 (s, 1H, Ar-*H*), 3.98 (t, 4H, *J* = 6.6 Hz, –OC*H₂*–), 1.89-1.77 (m, 4H, –OCH₂C*H₂*–), 1.54-1.43 (m, 4H, –C*H₂*–), 1.42-1.22 (m, 16H, –C*H₂*–), 0.94-0.84 (m, 6H, –CH₂C*H₃*). **¹³C-NMR** (75 MHz, CDCl₃): δ(ppm) = 155.6, 135.7, 103.0 ,99.8, 69.7, 31.8, 29.3, 29.2, 29.0, 25.9, 22.6, 14.1. **Mp** = 63 – 65 °C.

BrRS-12. ¹H-NMR (300 MHz, CDCl₃): δ(ppm) = 7.63 (s, 1H, Ar-*H*), 6.45 (s, 1H, Ar-*H*), 3.98 (t, 4H, *J* = 6.6 Hz, –OC*H₂*–), 1.88-1.77 (m, 4H, –OCH₂C*H₂*–), 1.54-1.41 (m, 4H, –C*H₂*–), 1.40-1.20 (m, 32H, –C*H₂*–), 0.87 (t, 6H, *J* = 6.6 Hz, –CH₂C*H₃*). **¹³C-NMR** (75 MHz, CDCl₃): δ(ppm) = 155.6, 135.7, 102.9 ,99.8, 69.7, 31.9, 29.7-29.5, 29.4, 29.3, 29.0, 25.9, 22.7, 14.1. **Mp** = 62 – 64 °C.

BrRS-18. ¹H-NMR (300 MHz, CDCl₃): δ(ppm) = 7.64 (s, 1H, Ar-*H*), 6.46 (s, 1H, Ar-*H*), 3.98 (t, 4H, *J* = 6.6 Hz, –OC*H₂*–), 1.88-1.77 (m, 4H, –OCH₂C*H₂*–), 1.56-1.18 (m, 60H, –C*H₂*–), 0.91-0.85 (m, 6H, –CH₂C*H₃*). **¹³C-NMR** (75 MHz, CDCl₃): δ(ppm) = 155.6, 135.7, 103.0, 99.8, 69.7, 31.9, 29.7-29.3, 29.0, 26.0, 22.7, 14.1. **Mp** = 79 – 81 °C.

BrRS-22. ¹H-NMR (300 MHz, CDCl₃): δ(ppm) = 7.64 (s, 1H, Ar-*H*), 6.46 (s, 1H, Ar-*H*), 3.98 (t, 4H, *J* = 6.5 Hz, –OC*H₂*–), 1.88-1.77 (m, 4H, –OCH₂C*H₂*–), 1.56-1.19 (m, 76H, –C*H₂*–), 0.91-0.84 (m, 6H, –CH₂C*H₃*). **¹³C-NMR** (75 MHz, CDCl₃): δ(ppm) = 155.6, 135.7, 103.0, 99.8, 69.7, 31.9, 29.7-29.5, 29.4, 29.3, 29.0, 25.9, 22.7, 14.1. **Mp** = 80 – 84 °C.

C) Bis-Formylation

Under an inert gas atmosphere, the brominated product was dissolved in dry THF and tetramethylethylenediamine (TMEDA, 3 eq) was added into the solution. The solution was then cooled to −78 °C and *n*-butyllithitum (5 eq) was slowly added at that temperature and stirred for 30 min. The solution was then allowed to warm up to room temperature and afterwards again cooled to −78 °C. DMF (7 eq) was added and the reaction mixture was allowed to reach room temperature overnight. The solution was quenched with saturated NH₄Cl solution and concentrated on rotary evaporator. The obtained solid was treated with water and the remaining solid filtered off. The solid was then purified by column chromatography (PE/Ethylacetate 95:5, v/v) to provide the desired product as light brown solid (yields around 40%).

¹H NMR,¹³C NMR, **HRMS** spectra and melting points of the final products.

IPA₁. ¹H-NMR (300 MHz, CDCl₃): δ(ppm) = 10.27 (s, 2H, –C*H*O), 8.34 (s, 1H, Ar-*H*), 6.45 (s, 1H, Ar-*H*), 4.03 (s, 6H, –OC*H₃*). **¹³C-NMR** (75 MHz, CDCl₃): δ(ppm) = 187.7, 167.4, 132.1, 119.0, 94.5, 56.3. Corresponds to the literature.[10]

IPA₄. ¹H-NMR (300 MHz, CDCl₃): δ(ppm) = 10.30 (s, 2H, –C*H*O), 8.34 (s, 1H, Ar-*H*), 6.41 (s, 1H, Ar-*H*), 4.14 (t, 4H, *J* = 6.4 Hz, –OC*H₂*–), 1.94-1.81 (m, 4H, –OCH₂C*H₂*–), 1.60-1.46 (m, 4H, –C*H₂*CH₃), 1.00 (t, 6H, *J* = 7.4

Hz, –CH$_2$CH_3). ^{13}**C-NMR** (75 MHz, CDCl$_3$): δ(ppm) = 187.7, 167.1, 131.0, 118.7, 95.4, 68.8, 30.9, 19.2, 13.7. **HRMS** (APCI$^+$) for C$_{16}$H$_{22}$O$_4$: calc. 279.1591 [M+H]$^+$; found 297.1593 [M+H]$^+$. **Mp** = 95 – 98 °C.

IPA$_8$. ^{1}**H-NMR** (300 MHz, CDCl$_3$): δ(ppm) = 10.31 (s, 2H, –CHO), 8.35 (s, 1H, Ar-H), 6.41 (s, 1H, Ar-H), 4.13 (t, 4H, J = 6.5 Hz, –OCH_2–), 1.94-1.82 (m, 4H, –OCH$_2$CH_2–), 1.56-1.22 (m, 20H, –CH_2–), 0.94-0.83 (m, 6H, –CH$_2$CH_3). ^{13}**C-NMR** (75 MHz, CDCl$_3$): δ(ppm) = 187.7, 167.1, 131.0, 118.7, 95.4, 69.1, 31.7, 29.2, 29.1, 28.8, 26.0, 22.6, 14.1. **HRMS** (APCI$^+$) for C$_{24}$H$_{38}$O$_4$: calc. 391.2843 [M+H]$^+$; found 391.2842 [M+H]$^+$. **Mp** = 75 – 78 °C.

IPA$_{12}$. ^{1}**H-NMR** (300 MHz, CDCl$_3$): δ(ppm) = 10.32 (s, 2H, –CHO), 8.36 (s, 1H, Ar-H), 6.41 (s, 1H, Ar-H), 4.13 (t, 4H, J = 6.7 Hz, –OCH_2–), 1.94-1.81 (m, 4H, –OCH$_2$CH_2–), 1.55-1.19 (m, 36H, –CH_2–), 0.88 (t, 6H, J = 6.6 Hz, –CH$_2$CH_3). ^{13}**C-NMR** (75 MHz, CDCl$_3$): δ(ppm) = 187.6, 167.1, 131.0, 118.7, 95.4, 69.1, 31.9, 29.63, 29.60, 29.55, 29.50, 29.33, 29.27, 28.9, 26.0, 22.7, 14.1. **HRMS** (APCI$^+$) for C$_{32}$H$_{54}$O$_4$: calc. 503.4095 [M+H]$^+$; found 503.4096 [M+H]$^+$. **Mp** = 77 – 80 °C.

IPA$_{18}$. ^{1}**H-NMR** (300 MHz, CDCl$_3$): δ(ppm) = 10.31 (s, 2H, –CHO), 8.36 (s, 1H, Ar-H), 6.41 (s, 1H, Ar-H), 4.13 (t, 4H, J = 6.5 Hz, –OCH_2–), 1.93-1.84 (m, 4H, –OCH$_2$CH_2–), 1.59-1.19 (m, 60H, –CH_2–), 0.90-0.85 (m, 6H, –CH$_2$CH_3). ^{13}**C-NMR** (75 MHz, CDCl$_3$): δ(ppm) = 187.7, 167.0, 131.0, 118.4, 95.4, 69.1, 32.9, 29.7, 29.5, 29.3, 28.9, 26.0, 22.7, 14.1. **HRMS** (APCI$^+$) for C$_{44}$H$_{79}$O$_4$: calc. 671.5973 [M+H]$^+$; found 671.5967 [M+H]$^+$. **Mp** = 90 – 93 °C.

IPA$_{22}$. ^{1}**H-NMR** (300 MHz, CDCl$_3$): δ(ppm) = 10.33 (s, 2H, –CHO), 8.37 (s, 1H, Ar-H), 6.42 (s, 1H, Ar-H), 4.14 (t, 4H, J = 6.5 Hz, –OCH_2–), 1.94-1.83 (m, 4H, –OCH$_2$CH_2–), 1.57-1.17 (m, 76H, –CH_2–), 0.91-0.84 (m, 6H, –CH$_2$CH_3). ^{13}**C-NMR** (75 MHz, CDCl$_3$): δ(ppm) = 187.7, 167.1, 131.1, 118.7, 95.4, 69.1, 31.9, 29.8-29.5, 29.4, 29.3, 28.9, 26.0, 22.7, 14.1. **HRMS** (APCI$^+$) for C$_{52}$H$_{94}$O$_4$: calc. 783.7225 [M+H]$^+$; found 783.7230 [M+H]$^+$. **Mp** = 100 – 102 °C.

1. A.J. Gellman, and A.R. Paserba. Kinetics and Mechanism of Oligomer Desorption From Surfaces: N-Alkanes on graphite. *J. Phys. Chem. B* 2002, 106, 13231─13241.

2. S. Yin, C. Wang, X. Qiu, B. Xu, and C. Bai. Theoretical Study of the Effects of Intermolecular Interactions in Self-assembled Long-chain Alkanes Adsorbed on Graphite Surface. *Surf. Interface Anal.* 2001, 32, 248─252.

3 J.D. Bernal, and B.W. Lawrence. The Structure of Graphite. *Proc. R. Soc. Lond. A* 1924, 106, 749─773.

4 J. Comer, J.C. Gumbart, J. Hénin, T. Lelièvre, A. Pohorille, and C. Chipot. The Adaptive Biasing Force Method: Everything You Always Wanted To Know but Were Afraid To Ask. *J. Phys. Chem. B* 2015, 119, 1129─1151.

5 J.P. Rabe, and S. Buchholz. Direct Observation of Molecular Structure and Dynamics at the Interface Between a Solid Wall and an Organic Solution by Scanning Tunneling Microscopy. *Phys. Rev. Lett.* 66, 2096─2099.

6. T. Okada, N. Fujiwara, T. Ogata, O. Haba, and M. Ueda. Synthesis of Regiocontrolled Poly(4,6-di-n-butoxy-1,3-phenylene) by Oxidative Coupling Polymerization. *J. Polym. Sci. A* 1997, 35, 2259─2266.

7. J. Chen, S. Ko, L. Liu, Y. Sheng, H. Han, and X. Li. The Effect of Different Alkyl Chains on the Photovoltaic Performance of D–π–a Porphyrin-sensitized Solar Cells. *New J. Chem.* 2015, 39, 3736─3746.

8. C.Y. Lee, and J.T. Hupp. Dye Sensitized Solar Cells: Tio2 Sensitization with a Bodipy-porphyrin Antenna System. *Langmuir* 2010, 26, 3760─3765.

9. L. Yang, Z. Lu, and S.S. Stahl. Regioselective Copper-catalyzed Chlorination and Bromination of Arenes with O$_2$ as the Oxidant. *Chem. Commun.* 2009, 6460─6462.

10. K. Benelhadj, J. Massue, and G. Ulrich. 2,4 and 2,5-bis(Benzooxazol-2′-yl)Hydroquinone (DHBO) and Their Borate Complexes: Synthesis and Optical Properties. *New J. Chem.* 2016, 40, 5877─5884.